Part V
CFD Analysis of a Complete Offshore Wind Turbine

Chapter 16
An Overview of the CFD Analyses in the MARE-WINT Project

George N. Barakos

Abstract In the MARE-WINT project, two early stage researchers, researched and developed CFD methods for complete offshore wind turbine configurations. This brief chapter provides an overview of the work conducted by these two fellows.

The subsequent two chapters detail the work carried out during the MARE-WINT project on the CFD simulation of complete wind turbines. The term 'complete' needs to be clearly defined, since it is used here only in relation to the current CFD state-of-the-art. Often, Wind Turbine (WT) blades are analysed using grid-based Navier–Stokes methods under the assumption of steady flow with spatial symmetry between blades. The inflow to the blades is uniform, the tower, spinner and nacelle are typically ignored and the aeroelastic effects are absent.

The work at MARE-WINT progressed beyond the current state-of-the art by presenting results for configurations that include all blades, the tower and nacelle, aeroelasticity and even the effect of the wind turbine motion due to waves for floating off-shore configurations. An additional feature of the current work is that large scale wind turbines are considered in contrast to past CFD works that mainly simulated scaled wind turbines used for validation of CFD against wind tunnel data.

Two fellows contributed to this task, and one common theme between their works is that they both used compressible CFD solvers. This was driven by two reasons. On one hand, the solvers were readily available and well-validated for high speed aerodynamic flows (compressible flows) like flows around transonic aerofoils, cascades, helicopter rotors etc. The methods used low-Mach and all-Mach schemes to account for the relatively low speed flow around wind turbines. Both methods used multi-block structured grids with sliding grids to account for the relative motion between blades and the tower. The solvers used turbulence models of the k-ω family for their work. The use of structured grids was combined with the use of aeroelastic methods. These fall within the established Fluid/Structure Interaction methods that are common in aerospace applications. The methods include not only modal-based representations of the blades but also mesh deformation, interpolation

G.N. Barakos (✉)
Division of Aerospace Sciences, School of Engineering, University of Glasgow,
James Watt South Building, Glasgow G12 8QQ, UK
e-mail: george.barakos@glasgow.ac.uk

W. Ostachowicz et al. (eds.), *MARE-WINT*, DOI 10.1007/978-3-319-39095-6_16

and motion methods to accommodate the dynamic change of the blade shape during its motion.

One of the researchers went even further by considering flaps on the blades as described in other paragraphs of this book. Furthermore, the CFD methods were coupled with a hydrodynamic method to allow for the simultaneous solution of the liquid domain near the water-surface of off-shore cases. Additional modelling elements worth of mention here, include the use of a multi-body dynamics tool to allow for the effect of mooring lines and the overall rigid motion of the complex WT system to be accounted for effectively. The use of multi-body simulation is common in the context of simpler engineering methods than CFD, where the blade-element momentum theory is used to estimate the blade loads but it has so far been unexplored for grid-based Navier–Stokes methods.

To close the introduction to this part it should be mentioned that more elaborate models of complete wind turbines would include a time-varying inflow as well as a model of the drive-train and the control system of the WT. These are extensions that should be attempted by the fellows of MARE-WINT in the future as their work progresses and their skills are advancing. Needless to mention here that the CFD analyses of the complete wind turbines are to benefit from parallel computing and especially the use of new processor technologies like Graphical Processing Units as well as many-core machines like the Intel phil.

Extrapolating from this work, one expects to see in the future, work on extreme and fatigue loads with CFD replacing some of the BEM methods that are now used due to the large number of cases necessary to be computed for the overall loads envelope of a WT. Additional applications will include active rotors with flaps and flow control systems, as well as, direct simulation of wind turbine noise. Farm analysis is also expected to move away from the free-wake and actuator disk LES-like simulations, to properly resolved blades with high order schemes able to capture and maintain wakes for the necessary length of time and space.

Chapter 17
CFD Investigation of a Complete Floating Offshore Wind Turbine

Vladimir Leble and George N. Barakos

Abstract This chapter presents numerical computations for floating offshore wind turbines for a machine of 10-MW rated power. The rotors were computed using the Helicopter Multi-Block flow solver of the University of Glasgow that solves the Navier-Stokes equations in integral form using the arbitrary Lagrangian-Eulerian formulation for time-dependent domains with moving boundaries. Hydrodynamic loads on the support platform were computed using the Smoothed Particle Hydrodynamics method. This method is mesh-free, and represents the fluid by a set of discrete particles. The motion of the floating offshore wind turbine is computed using a Multi-Body Dynamic Model of rigid bodies and frictionless joints. Mooring cables are modelled as a set of springs and dampers. All solvers were validated separately before coupling, and the loosely coupled algorithm used is described in detail alongside the obtained results.

Nomenclature

Latin

d	distance between particles (m)
I	inertia tensor (kg m^2)
m	mass (kg)
w	relative weight between the fluid and body particles (–)

Greek

α	artificial viscosity parameter (–)
γ	adiabatic index (–)

V. Leble • G.N. Barakos (✉)
Division of Aerospace Sciences, School of Engineering, University of Glasgow, James Watt South Building, Glasgow, G12 8QQ UK
e-mail: v.leble.1@research.gla.ac.uk; george.barakos@glasgow.ac.uk

W. Ostachowicz et al. (eds.), *MARE-WINT*, DOI 10.1007/978-3-319-39095-6_17

ω rotational velocity (rad/s)
τ gyroscopic torque (Nm)

Acronyms

BEM	Blade Element Momentum method
BILU	Block-Incomplete Upper Lower factorisation
FOWT	Floating Off-shore Wind Turbine
FSI	Fluid Structure Interaction
GCG	Generalised Conjugate Gradient
GMRES	Generalised Minimal Residual method
HMB3	Helicopter Multi-Block CFD Solver
HPC	High Performance Computer
IBQN-LS	Interface Block Quasi-Newton with an approximation for the Jacobian from a Least-Squares mode
IQN-ILS	Interface Quasi-Newton algorithm with an approximation for the inverse of the Jacobian from a Least-Squares model
MBDM	Multi-Body Dynamic Model
MPI	Message Passing Interface library
SPH	Smoothed Particle Hydrodynamics Method

17.1 Motivation and Objectives

Over the years, offshore wind farms have moved further from the shore and into deeper waters. At the end of 2014, the average water depth of grid connected wind farms was 22.4 m and the average distance to shore 32.9 km. Projects under construction, consented and planned confirm that average water depths and distances to shore are likely to increase (Arapogianni et al. 2013). Shallow water regions suitable for seabed-fixed, offshore wind turbines are limited, and for sea depths exceeding 30–60 m, floating structures become more economic. Hence, emphasis is placed on the development of floating offshore wind turbines (FOWTs) with several prototypes already operational across the world (Arapogianni et al. 2013). Unlike onshore machines, the FOWT is a highly dynamic system subjected to the wind and wave loads and only constrained by a mooring system. Further, the rotor frequency is low due to the large size of the blades, and wave frequencies may come close or coincide with the rotational frequency of the rotor. It is, therefore, important to develop a method for the analysis of this air-structure-water system.

The common approach is to combine simplified tools into one hybrid model to predict wind turbine responses under wind and wave loads. The Blade Element Momentum (BEM) method is frequently used to calculate aerodynamic loads on the blades and tower (Jonkman 2007; Skaare et al. 2007; Karimirad and Moan 2013).

Sometimes analytical models are used that take the form of algebraic equations for the applied thrust that is proportional to the area of the rotor and the relative velocity between the wind and the hub as in Roddier et al. (2009) and Karimirad and Moan (2012). If aero-elasticity is considered, it is often included in BEM methods, where the structure is described by a multi-body formulation, in which wind turbine structures are subdivided into a number of bodies and each body consists of an assembly of Timoshenko beam elements (Larsen and Hanson 2007). Another approach is to characterise flexible bodies using linear modal representation, which usually assumes small deflections.

The hydrodynamic loads on the support structure are often modelled with a linear potential theory assuming inviscid, incompressible and irrotational flow, also known as Airy wave theory (Jonkman 2007; Rieper 2011; Karimirad and Moan 2013). In this case, frequency dependent hydrodynamic-added-mass and hydrodynamic-damping matrices, along with wave-excitation force vector are precomputed for a given problem, and serve as input to the coupled model. At the beginning of the computation, the wave-radiation-retardation kernel is obtained by integrating user-supplied added-mass or damping coefficients (Jonkman 2007). This way, external computer routines can be linked to the aerodynamic solver as a function that employs convolution integrals and returns hydrodynamic loads at given instances. The non-linear hydrodynamic viscous drag is included from Morison's equation (Morison et al. 1950) using strip theory. The drag coefficient involved in Morison's equation is often determined based on experiments. Since the drag coefficient depends on many factors, including the Reynolds number, geometry, and the presence of a free surface and a free end of a body, the experimental data is not always directly applicable. The drag coefficient can be obtained from a CFD computation for given support platform and then applied to Morison's equation improving the results as was shown by Benitz et al. (2015).

Linearization of the hydrodynamic problem implies that the translational displacements of the support platform are small relative to the size of the body, and that amplitudes of the incident waves are much smaller than their wavelengths i.e. steep or breaking waves cannot be modelled. Some extensions to the second-order potential flow was performed e.g. by Marino et al. (2011) and Roald et al. (2013). Even with second-order hydrodynamic terms included, however, the potential hydrodynamic theory might not completely apply to floating wind turbine platforms due to the large displacements encountered (Matha et al. 2011). Mooring lines constraining the FOWT can be modelled using springs (Savenije et al. 2010), flexible beams (Skaare et al. 2007) or multi-body chains of rigid bodies (Matha et al. 2011). Sometimes, precomputed nonlinear force-displacement relationships are employed, as in Karimirad and Moan (2012). Some of the works in the field of FOWT modelling are summarised in Table 17.1.

The purpose of this chapter is to present a coupling algorithm that brings together two Naver-Stokes solvers. For this, the Helicopter Multi-Block (HMB3) solver (Barakos et al. 2005) is used to solve for the aerodynamic forces acting on the wind turbine (WT) blades. Hydrodynamic forces on the support platform are solved using the Smoothed Particle Hydrodynamics (SPH) method (Gomez-Gesteira et al. 2012;

Table 17.1 Works relevant for the complete FOWT models

Author(s)	Aerodynamic method	Hydrodynamic method
Jonkman (2007)	BEM	Linear potential
Skaare et al. (2007)	BEM	Linear potential
Roddier et al. (2009)	BEM	Linear potential
Karimirad and Moan (2013)	BEM/Analytical	Linear potential/Second-order potential/Morison's equation

Woodgate et al. 2013). Both solvers are coupled by exchanging information while the FOWT is represented by a lumped mass model.

17.2 Numerical Methods

HMB3 is a 3D multi-block structured solver for the Navier-Stokes equations in 3D. HMB3 solves the Navier-Stokes equations in integral form using the arbitrary Lagrangian-Eulerian formulation for time-dependent domains with moving boundaries (Dehaeze and Barakos 2012a, b; Carrión et al. 2014a). The solver uses a cell-centred finite volume approach combined with an implicit dual-time method (Jameson 1991). Osher's upwind scheme (Osher and Chakravarthy 1983) is used to resolve the convective fluxes. Central differences (CD) spatial discretisation is used for the viscous terms. The non-linear system of equations that is generated as a result of the linearization is solved by integration in pseudo-time using a first-order backward difference method. A Generalised Conjugate Gradient (GCG) method is then used (Eisenstat et al. 1983) in conjunction with a Block Incomplete Lower-Upper (BILU) factorisation as a pre-conditioner (Axelsson 1994). The HMB3 solver has a library of turbulence closures including several one- and two- equation models. Turbulence simulation is also possible using either the Large-Eddy or the Detached-Eddy simulation approach (Spalart et al. 1997). The solver was designed with parallel execution in mind and the MPI library along with a load-balancing algorithm are used to this end. The flow solver can be used in serial or parallel fashion for large-scale problems. Depending on the purposes of the simulations, steady and unsteady wind turbine CFD simulations can be performed in HMB3 using single or full rotor meshes generated using the ICEM-Hexa tool. Rigid or elastic blades can be simulated using static or dynamic computations. HMB3 allows for sliding meshes to simulate rotor-tower interaction cases as described in Steijl and Barakos (2008). Alternatively, overset grids can be used with the details presented in Jarkowski et al. (2013). To account for low-speed flows, the Low-Mach Roe scheme (LM-Roe) developed by Rieper (2011) is employed for wind turbine cases (Carrión et al. 2013). The chosen methodology allows for easy updating of the solver with new functions. One example presented here, is the coupling with a hydrodynamic solver.

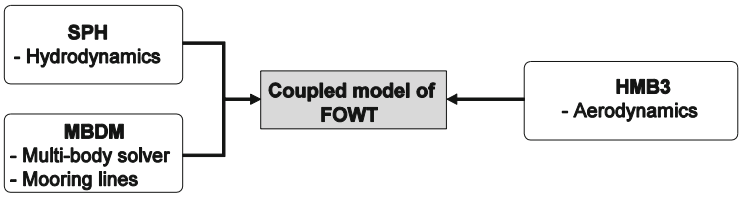

Fig. 17.1 Schematic of the solvers employed in the floating offshore wind turbine model

The sea is modelled with the SPH method (Gomez-Gesteira et al. 2012). Each SPH particle has individual material properties and moves according to the Navier-Stokes equations solved in the Lagrangian form. SPH offers a variety of advantages for fluid modelling, particularly those with a free surface and moving bodies. Due to the Lagrangian nature of the SPH method, the free surface requires no special treatment. Further, submerged bodies can be represented with particles. Therefore, it is natural for the method to include floating objects.

The motion of the FOWT components is computed with a multi-body model (MBDM) of rigid bodies and frictionless joints. Mooring cables are modelled as a set of springs and dampers, according to Savenije et al. (2010). The coordinate partitioning method of Nikravesh (1988) is used to solve the resulting system of mixed differential-algebraic equations. The time integration scheme for independent variables is explicit and various schemes are implemented up to the Runge-Kutta method of fourth order. The non-linear position equations for dependent variables are solved using the Newton-Raphson method with exact, an analytical, Jacobian.

The current implementation is schematically presented in Fig. 17.1, where coupling is between both fluids. Another option would be to employ a multi-phase solver (e.g. Volume of Fluid as in Beyer et al. (2013)). This approach does not tackle the problem of coupling, but shifts it to the structure-fluid side.

17.2.1 Validation of the Aerodynamic Solver

The HMB3 CFD solver has so far been validated for several wind turbine cases, including the NREL Annex XX experiments (Gómez-Iradi et al. 2009), where the effect of the blades passing in front of the tower was captured, as can be seen by the deficit of the thrust values presented in Fig. 17.2a. The under-prediction of 3 % is due to the fact that computations were performed at the nominal conditions for the experiment, and not for the measured pitch. A small change of pitch accounts for this difference. The pressure and PIV data of the MEXICO project (Schepers and Snel 2007, 2012) have also been used for validation (Carrión et al. 2014b), where the wake was resolved on a fine mesh capable to capture and preserve the vortices downstream the rotor (Fig. 17.2), which enabled the prediction of the onset of wake instabilities (Carrión et al. 2015).

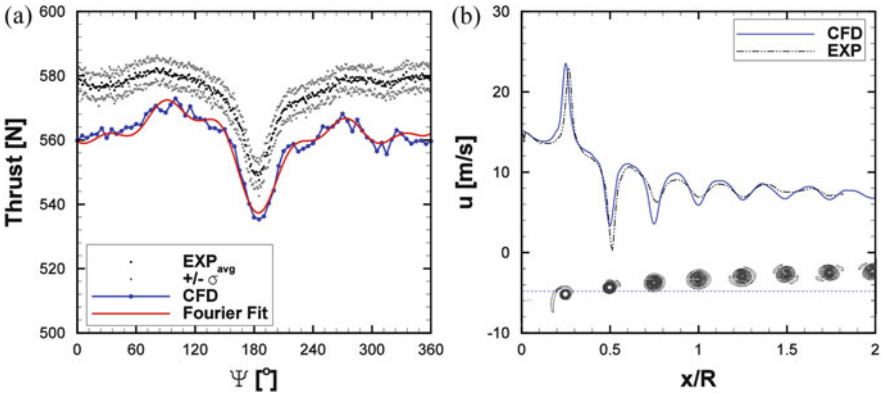

Deficit in thrust of the NREL Annex XX blade when passing in front of the tower with corresponding Fourier series fit of five modes.

Axial velocity profile passing through the first vortex generated by the MEXICO blade.

Fig. 17.2 Thrust prediction over a full revolution of the NREL Annex XX wind turbine at 7 m/s wind speed (**a**); and prediction of MEXICO rotor wake, including axial velocity profile (**b**) (Carrión et al. 2015)

17.2.2 Validation of the Hydrodynamic Solver

The hydrodynamic loads are estimated using the SPH method validated against the experiments of Greenhow and Lin (1983) for the high speed entry of a half-buoyant solid cylinder into calm water. As shown in Fig. 17.3a a cylinder of density of 500 kg/m^3 was allowed to fall freely from the height of 0.8 m under gravity acceleration; the water depth was 0.3 m. The density of the cylinder was assigned by defining the relative weight between fluid and cylinder particles to be $w = 0.5$. Simulations were run with a cubic spline kernel, artificial viscosity with viscosity parameter $\alpha = 0.1$, adiabatic index $\gamma = 7$, and Courant-Friedrichs-Lewy number CFL = 0.2. The viscosity between the cylinder SPH particles and the fluid particles was neglected. Five cases were compared with different distances d between the particles. The penetration depth of the cylinder for all cases, along with the experimental results, are shown in Fig. 17.3b, whereas Fig. 17.4 shows the water surface deformation. The results were used for estimating the particle density and viscosity necessary for computations of floating bodies. Note that the best agreement with the experiment was obtained with distances between the particles d = 0.23 cm, what corresponds to 25 particles per radius of the cylinder.

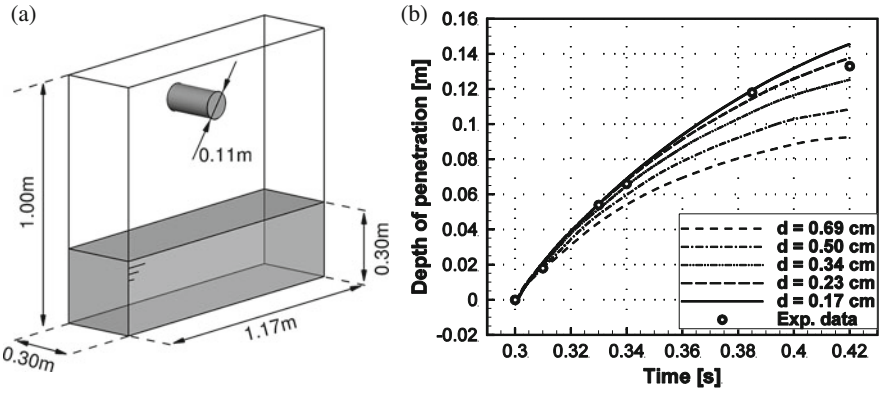

Schematic of the SPH validation setup. View of the whole domain.

Depth of penetration of a cylinder.

Fig. 17.3 Validation case for the SPH solver. (**a**) Schematic of the SPH validation setup; (**b**) Depth of penetration of a cylinder of density 500 kg/m^3: SPH results for different distances between particles *d* and experimental results of Greenhow and Lin (1983)

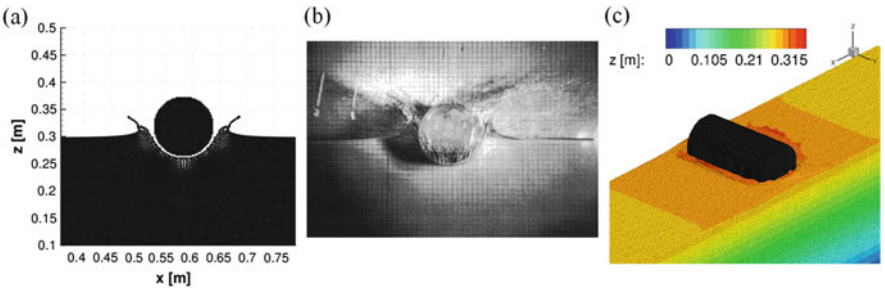

Cross section view.

Experiment.

Isometric view.

Fig. 17.4 Surface deformation during water entry of a cylinder for time t = 0.32s from the beginning of the fall. Comparison between CFD results with distance d = 0.23 m between particles

17.2.3 Validation of Multi-body Dynamics Solver

The MBDM was validated using simple mechanical systems of known solution as presented in Leble and Barakos (2016) like 2D and 3D slider-crank mechanisms. The gyroscopic wheel mechanism was used to validate that the gyroscopic effect is properly accounted for in the multi-body formulation. The ground body was placed at the origin at the global coordinate system. A short rod of length 0.1 m was attached to the ground body at height 1.0 m using a universal joint. The other end of the rod was connected to the centre of mass of the steel wheel with a revolute joint. A constant rotational speed of 60 rad/s was applied to the wheel by a revolute driver.

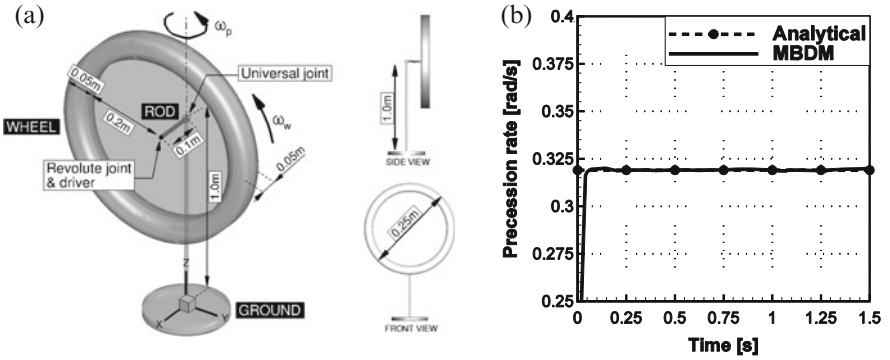

Schematic of the MBDM gyroscopic setup. Rate of precession.

Fig. 17.5 Validation of the MBDM to account for the gyroscopic effect. Test case setup (**a**), and rate of precession of the wheel (**b**)

Table 17.2 Properties of the bodies employed to model the gyroscopic effect

Name	Mass (kg)	Inertia tensor (kg m^2)
Wheel	28.3	$\begin{bmatrix} 1.45 & 0 & 0 \\ 0 & 0.73 & 0 \\ 0 & 0 & 0.73 \end{bmatrix}$
Rod	0.1	$\begin{bmatrix} 10^{-6} & 0 & 0 \\ 0 & 8.3 \times 10^{-5} & 0 \\ 0 & 0 & 8.3 \times 10^{-5} \end{bmatrix}$

The gravitational force acting in negative z direction was applied to all bodies, and at time t = 0 system was assumed to have no precession.

The system is presented in Fig. 17.5a, while the mechanical properties of all bodies are shown in Table 17.2. The analytical solution was obtained from Eq. (17.1) using the gyroscopic approximation, i.e. assuming that precession is much slower than rotation of the wheel $\omega_p \ll \omega_w$, so that the magnitude of the angular velocity $\left|\overrightarrow{\omega}\right| \cong |\omega_w|$ and that precession and rotation rates are nearly constant. Eq. (17.1) is shown below:

$$\omega_p = \tau / L = m_w g l / I_{xx} \omega_w \tag{17.1}$$

In Eq. (17.1), ω_p is the angular velocity of precession, τ is the moment due to gravity about the pivot point, and L is the angular momentum of the wheel. The expansion to the right-hand side involves the mass of the wheel m_w, the length of the rod l, the gravitational acceleration g, the mass moment of inertia of the wheel about the axis of rotation I_{xx}, and the rotational velocity of the wheel ω_w. Substitution of values from Table 17.2 into Eq. (17.1) yields the rate of precession as $\omega_p \approx 0.319$ rad/s. The results are presented in Fig. 17.5b, where the Runge-Kutta

integration scheme of fourth order was employed, with a time step $\Delta t = 0.0001s$. As can be seen, the rate of precession developed in less than 0.05s, and then maintained almost constant value that agreed with the one obtained using the gyroscopic approximation.

17.2.4 Coupling Algorithms

Coupling problems arise in many engineering problems, like fluid-structure interaction (FSI), but can also result from domain decomposition, where each sub-domain employs different discretisation or is solved with different method (Zienkiewicz et al. 2005). A multi-physics problem with adjacent domains can be simulated in a monolithic or in partitioned way. The former refers to the flow equations and structural equations being solved simultaneously, while the latter means that they are solved separately. The monolithic approach requires a specific solver for each particular combination of physical problems, whereas the partitioned approach allows for solver modularity. The partitioned approach also allows one to solve the fluid equations with different techniques developed specifically for the air and water. Further, this approach reduces the computational complexity per time-step, simplifies explicit/implicit treatment, facilitates sub-cycling, and eases replacements when better mathematical models and methods emerge in the fluid sub-disciplines. On the other hand, the partitioned simulation requires a special treatment to account for the interaction between the involved domains. Hence, computational efficiency over a monolithic approach is not necessarily guaranteed (Fellipa et al. 1999). The monolithic solution—which is the ultimate form of strong coupling, does not recognise the differences between the mathematical properties of the subsystems. Furthermore, it tends to ignore the issues of software modularity, availability, and integration, even though each of these issues can be in practice a major obstacle (Farhat et al. 2006). Considering that two available and validated solvers (HMB3 and SPH) can be used in this work, the emphasis is placed on partitioned algorithms.

Partitioned coupling can be weak or strong. Explicit algorithms are weak (or loose) as the solvers exchange information once per time step, and the coupled equations are not exactly satisfied due to explicit treatment. Depending on the formulation, one side of the coupling boundary conditions is usually lagging behind another. This can be improved with staggering or extrapolation techniques, but the scheme remains weak, and coupling errors may be introduced. However, loosely coupled algorithms are attractive, since among all solution methods, they are the simplest to implement for realistic applications, and the most computationally inexpensive per time step.

Implicit algorithms are strong (or tight), and enforce exactly the coupling conditions at each time level. This is obtained by conducting iterations until boundary equations are satisfied to certain, prescribed accuracy. The coupling problem can be formulated either as fixed-point or root-finding problem. For the former, fixed-point Jacobi or Gauss-Seidel methods can be employed. Although easy to implement,

those methods converge slowly if at all. Under-relaxation techniques can be used to improve convergence of the fixed-point iterations. Methods like fixed under-relaxation, adaptive Aitken's under-relaxation or steepest descent relaxation are some of the possible choices (Küttler and Wall 2008; Degroote et al. 2010). Newton's method can also be used. This method requires Jacobians relating the solutions of both solvers that are usually not known. This can be circumvented by employing approximation of Jacobian or Jacobian-vector product. Those types of coupling methods are called Quasi-Newton. Recently, new strongly coupled algorithms have been proposed.

Vierendeels et al. (2007) proposed an Interface Quasi-Newton algorithm with an approximation for the inverse of the Jacobian from a Least-Squares model (IQN-ILS). This approach was further investigated by Degroote et al. (2010), where they compared its performance with the Interface Block Quasi-Newton with an approximation for the Jacobian from a Least-Squares model (IBQN-LS), Aitken relaxation, and the Interface Generalised Minimal Residual method (Interface-GMRES(R)) algorithms. Demonstrated results showed that IQN-ILS and IBQN-LS performed similarly, using three times less evaluations and converging four times faster than the Aitken's relaxation method. IQN-ILS and IIBQN-LS were also found to use two times less evaluations and be almost three times faster than the Interface-GMRES algorithm.

Fernández and Moubachir (2005) reformulated fluid-structure interaction as a non-linear problem in the state of the structure, with the flow states considered as internal variables of the problem. This system was subsequently solved with the Newton-Raphson method using an exact Jacobian. The performance of this algorithm was compared with the performance of the Aitken relaxation and Quasi-Newton GMRES methods, for the inviscid flow in an elastic tube. Results showed that Aitken's relaxation was twice as slow as the Quasi-Newton and the exact Jacobian methods, and required almost 40 times more iterations. Further, for time steps of $\Delta t = 10^{-4}$ s, both latter algorithms showed similar behaviour in convergence. However, for time steps of $\Delta t = 10^{-3}$ s, the fixed-point and Quasi-Newton algorithms failed to converge. This implies sensitivity of the methods to the employed Jacobian.

The strong coupling may be important if the phenomena occurring in both fluids have similar time scales. Due to frequency similarities, resonances may occur and the exact response of a system will deviate from what is predicted by a loosely coupled algorithm. On the other hand, if time scales are largely different, loosely coupled algorithm may be sufficient. The exact bounds when the strong coupling is required for particular FOWT must be carefully assessed. Some indication comes from the waves and rotor frequency analysis. The sea state, wave height, wave frequency, and wind speed are empirically related in terms of range and most probable values e.g. in Lee et al. (1985). On the other hand, every wind turbine is designed to operate at a particular rotational frequency for a given wind speed. This allows one to construct a "Campbell" diagram for the FOWT investigated in this work (Fig. 17.6). It is clear that for sea states between 3 and 4 (or wind speed about 9 m/s) resonances may occur. The rated power production for this 10-MW

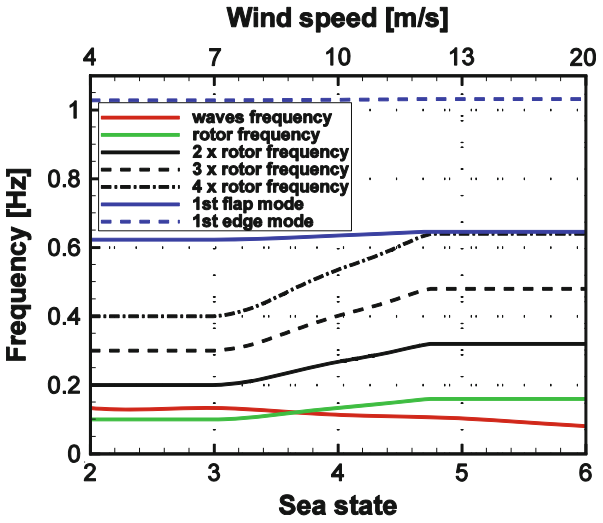

Fig. 17.6 Campbell diagram for the investigated FOWT showing frequencies of the rotor and the waves as function of sea state and wind speed

FOWT corresponds to the wind speed of 11.4 m/s, or sea state 4. This indicates that for rated conditions, the weakly coupled algorithm may be sufficient.

17.2.5 Coupling Scheme and Its Implementation

In general, the exchange of information without stopping the computations can be implemented in three ways: through files, shared memory or the Message Passing Interface (MPI). Writing a file is the simplest solution. Both solvers can be launched separately and write files whenever exchange of information is required. This approach calls for very minor changes to both codes.

In the shared memory approach multiple processes have access to the same memory, allowing them to change it and read changes made by other processes. If the random access memory (RAM) is to be used, it requires a shared memory machine, which may not be available on a general High Performance Computer (HPC). The file system can be used instead by mapping the memory on the hard drive. This approach suffers from the same drawback as the case of writing files. That is, writing and reading from hard drive creates a bottleneck, and slows down the computation especially if information is exchanged often, and large amount of data is to be exchanged.

Both employed CFD solvers are parallelised using MPI and the Single Program, Multiple Data (SPMD) paradigm, where each instance of the solver is assigned to perform the same task on different sets of data. Therefore, the easiest way to

combine solvers is to employ MPI, but in Multiple Program, Multiple Data (MPMD) approach, where different programs operate on different sets of data.

However, direct MPMD implementation of SPMD solvers requires additional effort to split the global communicator, such that each of the solvers is in a separate communicator (MPI COMM WORLD) with a separate ordering of processes, as detailed in Castain et al. (2015). This can be avoided by dedicating one process to be in charge of executing both solvers with MPI_Comm_spawn routine.

In the present work, the communication between the solvers was established through the Message Passing Interface (MPI), where the MBDM is executed as a single process and is dedicated to start SPH and HMB3 parallel solvers. The data flow diagram of the implementation is presented in Fig. 17.7.

The communication was validated by executing separately SPH or HMB3 and comparing with the results were the body motion was introduced by MBDM. Due to the Lagrangian nature of the SPH method, the submerged bodies can be represented with particles and do not require specific coupling. Therefore, by utilising MPI, the MBDM substituted the body motion routines of the SPH solver and reduced the number of coupled codes to two—SPH and HMB3. This implies that MBDM is advancing in time with the same integration scheme as SPH using a symplectic method in this case (Leimkuhler et al. 1996).

In the present work, a weakly coupled approach is employed, namely the parallel, conventional, staggered method shown in Fig. 17.8. Both solvers are advancing with different but constant time steps. SPH employs a time step of $\Delta t_{SPH} = 2 \times 10^{-4}$ s with CFL = 0.2, whereas HMB3 employs a time step of $\Delta t_{HMB3} = 2 \times 10^{-2}$ s $= 100 \Delta t_{SPH}$ with implicit CFL = 5.0. The small time step for the SPH method is required by the explicit integration scheme. The HMB3 solver employs an implicit dual-time method by Jameson (1991) that is superior for larger time steps. Synchronisation of the solvers is performed at the end of each HMB3 step.

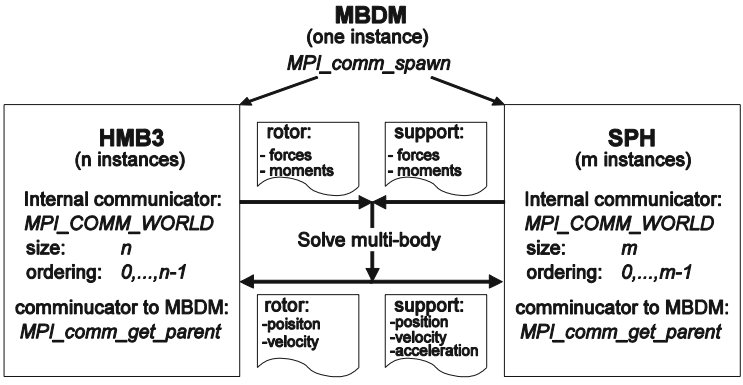

Fig. 17.7 Flow chart of the MPI implementation and data exchange for coupled model

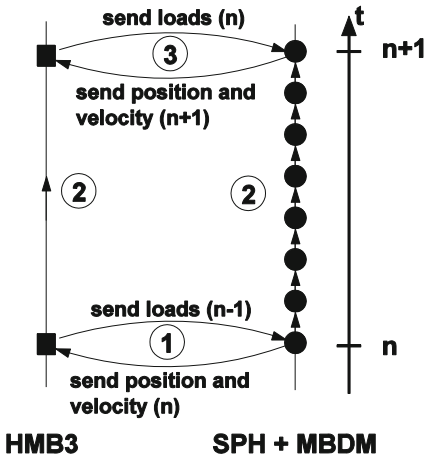

Fig. 17.8 The parallel conventional staggered method employed in present work

At the beginning of each synchronisation time step, the position and velocities of the rotor are transferred to the HMB3 aerodynamic solver, and forces and moments on the rotor are passed to the SPH. The two solvers are then advancing to a new time level with different methods and different number of steps. SPH performs 100 symplectic steps, while HMB3 performs 350 implicit pseudo-time steps. During the symplectic steps of the SPH code, the aerodynamic loads are kept constant (frozen). In return, the position and velocities of the rotor are kept constant during the implicit steps of HMB3. Once the synchronisation point is reached, the new position and velocities of all bodies, and rotor loads are obtained. Then, the algorithm proceeds to the new time level and information between the solvers is exchanged.

17.3 Test Case Description

A 10-MW wind turbine design by Bak et al. (2013) was used in this work. The blade consists of the FFA-W3 aerofoil family (Björck 1990) with the thickness ranging from 24 to 60 % of the chord. The blade has a non-linear distribution of the chord, the relative thickness of the section and the twist. The rotor diameter is 178.3 m, and the wind turbine operates at a wind speed of 11 m/s with a rotational speed of 8.8 rpm. The blades have a pre-coning of 2.5° and nonlinear pre-bending with 3.3 m displacement at the blade tip. The mass of the rotor is 228 tons, whereas mass of the nacelle and tower is 446 tons and 605 tons, respectively. The tilt of the nacelle in the original design is 5° nose up, but this was not included in the present model.

The wind turbine is attached to the floating support which consists of three cylindrical floats that increase the buoyancy and stability of the structure. A similar concept of the support platform was investigated by Roddier et al. (2009). Unlike

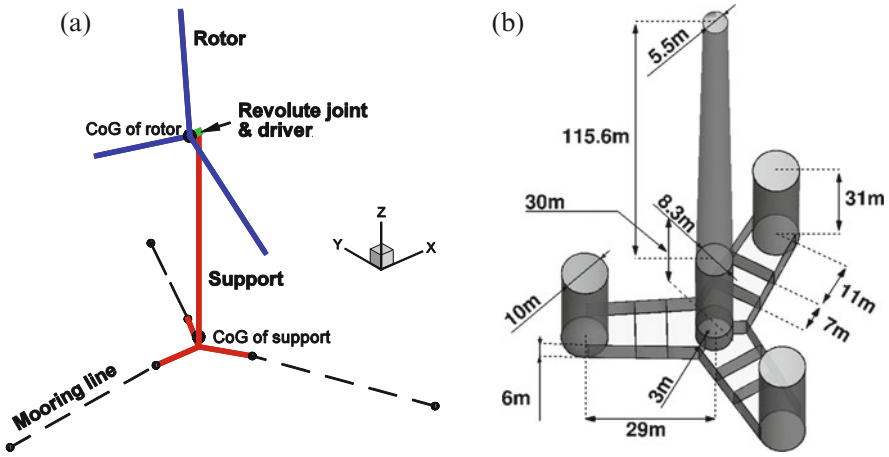

Schematic of the MBDM model of FOWT.

Dimensions of the support and tower.

Fig. 17.9 Schematic of the employed model of FOWT (**a**), and dimensions of the semi-submersible support and tower (**b**). FOWT model consists of three mooring lines and two rigid bodies: the rotor (*blue*) and combined body representing nacelle, tower and support (*red*). Adapted from Leble and Barakos (2016)

that design, the present support is simplified to be symmetric with respect to the location of the tower and the floats are connected to the base of the tower with a solid frame. The size of the tower is taken from Bak et al. (2013), and the dimensions of the support were calculated to provide sufficient buoyancy. A schematic of the studied FOWT is shown in Fig. 17.9.

In the present model, the FOWT is represented by three mooring lines and two bodies, as shown in Fig. 17.9a. The first body represents the rotor (three blades with the spinner), and the second body represents the combined nacelle, tower and floating support rigidly linked to each other. The two bodies are connected by a revolute joint and a constraint of constant rotational speed is applied to the rotor. The resulting system has 6 unconstrained degrees of freedom. The mechanical properties of the bodies and mooring lines are presented in Table 17.3.

The FOWT is placed in a shallow tank of length 500 m, width 150 m and height 30 m. The tank is filled with water to a depth of 20.6 m. The waves are generated using a paddle on one side, and dissipated using a beach-like slope on the other side of the tank. The tank is presented in Fig. 17.10. Waves are generated to represent the specific sea state corresponding to a given wind speed. Based on the measurements of annual sea state occurrences in the North Atlantic and North Pacific (Lee et al. 1985), the wind speed of 11 m/s corresponds to a sea state 4 with a mean wave height of 1.88 m and a period of 8.8 s.

Table 17.3 Mechanical properties of the employed bodies and mooring lines

Rotor	
m (kg)	227,962
I (kg m^2)	$\begin{bmatrix} 1.56\times10^8 & 0 & 0 \\ 0 & 7.84\times10^7 & 0 \\ 0 & 0 & 7.84\times10^7 \end{bmatrix}$
Nacelle, support and tower	
m (kg)	4,223,938
I (kg m^2)	$\begin{bmatrix} 2.03\times10^{10} & 0 & 0 \\ 0 & 2.03\times10^{10} & 0 \\ 0 & 0 & 2.81\times10^9 \end{bmatrix}$
Mooring lines	
120.0	Angle between adjacent lines ()
20.6	Depth of anchors below SWL (m)
7.0	Depth of fairleads below SWL (m)
116.73	Length of the relaxed line (m)
400×10^6	Mooring line extensional stiffness (N/m)
40,000	Mooring line damping coefficient (Ns/m)

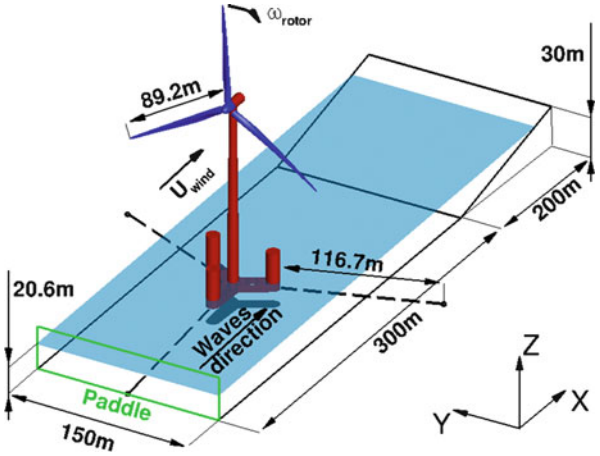

Fig. 17.10 The FOWT model placed in a shallow tank. Mooring lines are shown with *dashed lines*. Adapted from Leble and Barakos (2016)

17.3.1 CFD Mesh

The aerodynamic grid consists of the rotor and nacelle i.e. the tower is not included and the effect of the blade passing on the tower is not investigated. The grid consists of 8M cells, where 24 cells are used in the first layer, and 166 cells are distributed around the aerofoil section as presented in Fig. 17.11a. The surface of the blade is resolved with 90 cells along the span, as shown in Fig. 17.11b. The size of the first cell in the direction normal to the surface was 10^{-5}c, where c = 6.2 m is the

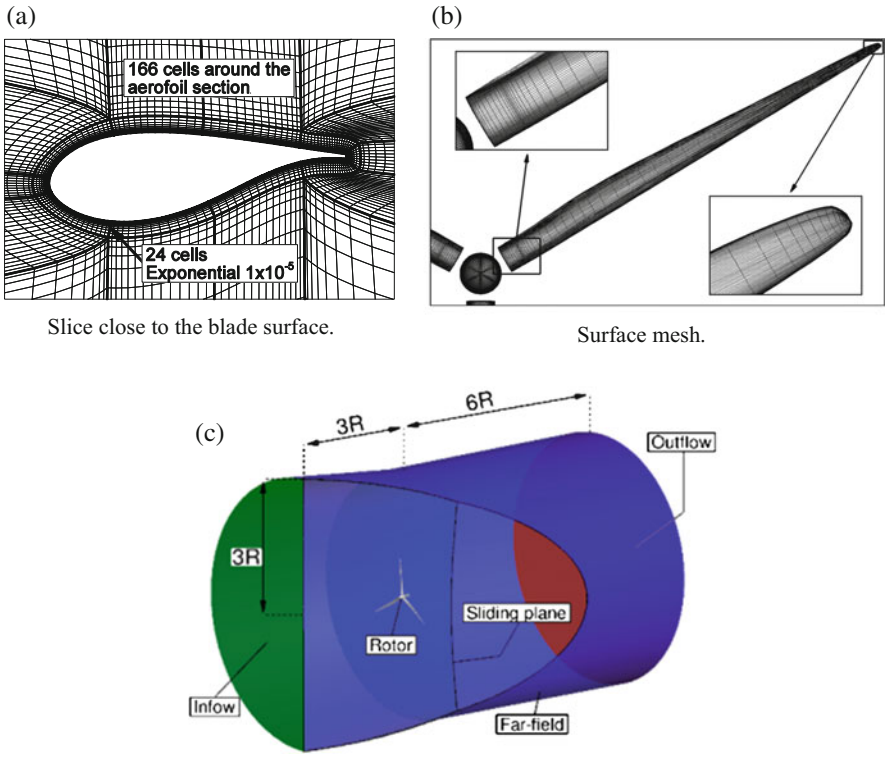

Fig. 17.11 8M mesh used to solve for aerodynamic loads. Slice through the volume close to the blade surface (**a**), surface mesh (**b**), and computational domain (**c**)

maximum chord of the blade. Based on the free-stream condition and the size of the first cell, the y + parameter was estimated to be y + = 1.2. It must be noted that the grid was relatively coarse as compared with the one used by Carrión et al. (2015) to capture the wake of the MEXICO rotor. However, a grid convergence study showed that this density is sufficient to produce meaningful, grid-independent results.

The density of the air was assumed to be $\rho = 1.225\,\text{kg/m}^3$, the dynamic viscosity of the air was assumed to be $\mu = 1.8 \times 10^{-5}\,\text{Ns/m}^2$, and the speed of sound was assumed to be 340 m/s. Further, the k-ω SST turbulence model was employed with the free-stream level of turbulence at 2.6 %. The flow was assumed to be fully turbulent, and the atmospheric boundary layer was not modelled. The uniform inflow boundary was set 3R upstream of the rotor, and the outflow boundary was set 6R downstream of the rotor, where R is the radius of the blade. The far-field boundary was assigned 3R from the centre of rotation. In addition, the sliding plane was used to connect rotor to the nacelle and allow relative motion. The computational domain with corresponding boundaries, a slice through the mesh

close to the blade surface, and the surface mesh of the blade are presented in Fig. 17.11.

17.3.2 SPH Setup and Resolution

The hydrodynamic domain is resolved using 5M particles with initial uniform spacing of d = 0.625 m. Note that the best agreement with experimental data was obtained for 25 particles per radius of the cylinder, as shown in Sect. 17.2.2. Here, the employed spacing corresponds to 9 particles per radius of the cylindrical leg, or to spacing d = 0.69 cm in Fig. 17.3b. The coarse particle distribution was chosen for economies in CPU time, where coarse domain is obviously solved faster, but tends to under-predict the slamming loads on the structure. Three test were performed to investigate the influence of the domain width and particle spacing on the force acting on the support structure, as presented in Table 17.4. The average hydrodynamic forces acting on the support during 1 s of simulation were used for comparison. This time interval was chosen such that it leads to direct comparison of the average loads per unit of time. Percentage difference is computed relative to the size and spacing employed for the coupled computation. As can be seen, the size of the hydrodynamic domain has little effect on the average hydrodynamic force. On the other hand, improving the spatial resolution results in about 18 % difference in the hydrodynamic force. This agrees with observations made in Sect. 17.2.2. A spacing of d = 0.3125 m would have been better, but to improve computational performance a spacing of d = 0.625 m was employed.

17.3.3 Initial Conditions

Each of the solvers was executed separately before coupling to obtain a periodic solution of the loads. During this phase of computation the floating support was fixed, and the waves were generated for approximately 30 s. The rotor was set to spin about the axis aligned with the direction of the incoming wind, and was first solved using HMB3 "hover" formulation with 20,000 steps during which the L2 norm of the residual vector dropped below 10^{-6}. Then, the unsteady computation was

Table 17.4 Test cases investigating the influence of the domain width and particle spacing on the forces acting on the support structure

Domain size x × y (m)	Spacing d (m)	1s averaged hydrodynamic force (N)	Difference (%)
500 × 150	0.6250	1.070×10^7	–
500 × 300	0.6250	1.068×10^7	0.20 %
500 × 150	0.3125	1.267×10^7	18.40 %

initiated and the flow was solved for an additional 30° of azimuth. The aerodynamic loads were almost constant during unsteady computation. Once the initial conditions were obtained, the coupled computations were initiated.

17.3.4 Demonstration Cases

The first demonstration case of the FOWT has the described configuration (see Fig. 17.10) with the difference that rotor was not included in multi-body formulation. Instead, the mass of the rotor was concentrated in the centre of gravity of the support to produce correct mass of the floating structure. In this way, the shift of the centre of mass due to rotor overhung was not considered. Further, the rotor inertia was not included, and the associated gyroscopic effects were not taken into account. The importance of these effects for the system at hand is assessed in the results section. Calm sea was considered, and the time varying thrust with the mean value of 1500 kN was applied at the location of the rotor. The thrust variation is shown in Fig. 17.12, and was estimated from a separate CFD computation of the rotor with the tower included.

This test case was solved for 150 s. Note that the demonstration case is not a coupled simulation, since the thrust force is prescribed and independent of the platform motion. The last test case was a coupled computation, as described in Sect. 17.2.5. This case was solved for 60 s, and allowed for almost 7 wave passages and about 9 revolutions of the rotor.

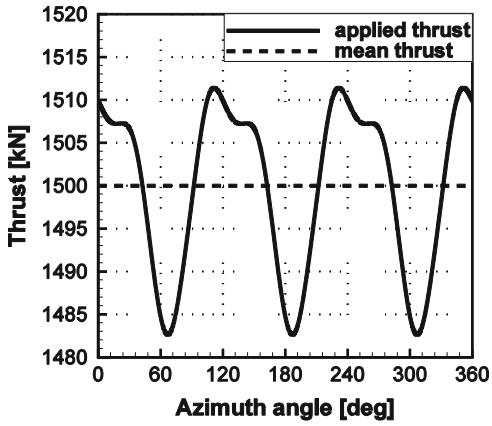

Fig. 17.12 Thrust as function of azimuth angle of the rotor for decoupled case

17.4 Results and Discussion

17.4.1 Decoupled Case

The results of the first case are presented in Fig. 17.13. As can be seen, the FOWT moves in the direction of the thrust by about 0.215 m (displacement in x). The FOWT also sinks in the water for about 0.603 m (displacement in z), and tends to settle at a pitch angle of around 0.09 rad or 5.2° (rotation about y axis). The SPH particles are settling for the first 15 s as is visible in the acceleration plot. This cannot be avoided even if the floating body is fixed and particles are let to settle. This is because releasing the floating structure is equivalent to a drop, and therefore does not represent equilibrium.

The last 20s of lateral and rotational accelerations are presented in Fig. 17.14. The effect of time varying thrust on the angular acceleration in pitch (about y axis) can be seen in Fig. 17.14c. The variation in the shape and frequency corresponds to the applied time dependent thrust. The effect of time varying thrust on the lateral accelerations can be seen in Fig. 17.14. Again, the frequency of accelerations corresponds to the frequency of the thrust, but some phase shift is present and the shape of the response does not follow the shape of the thrust. This is because the motion in heave is linked to the applied thrust only through the rotational motion of the support i.e. through the second time integral of the angular acceleration that does follow the shape of the thrust as shown in Fig. 17.14c.

The acceleration in the x direction is directly linked to the applied thrust, and the frequency dependence on thrust without the phase shift is clearly visible. However, the shape of the acceleration is not following the shape of applied thrust. This is a result of high stiffness of the mooring lines in this direction, where high frequency response of the mooring system augments the overall response of the support platform.

There are three sources of momentum for the decoupled computation: hydrodynamics, prescribed aerodynamics and mooring lines. Time histories of forces and moments are presented in Fig. 17.15. Note that for clarity, the time starts at 25 s. Also, note the differences in magnitude of the computed moments, where moments about y axis are three orders of magnitude bigger, as compared to the other moment components.

First, it should be noted that mooring lines are in general opposing the hydrodynamic forces introduced by the SPH solver. This is not true for the pitching moment, where hydrodynamics and mooring lines are acting together to counter the imbalance of the moment due to the thrust. For the mooring lines, moment is created by the displacements of the fairleads, whereas for the hydrodynamics, moment is created by the change of the buoyancy introduced by the rotation of the support. As can be seen, the mooring lines contribute about 30 %, whereas buoyancy about 70 % of the restoring moment in this system. One would expect similar, cooperative behaviour for the forces in surge (in x direction). The obtained

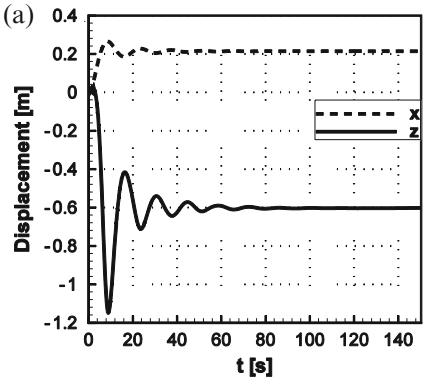

Displacement of centre of gravity.

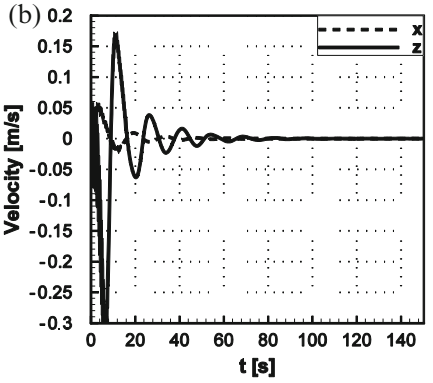

Velocity of centre of gravity.

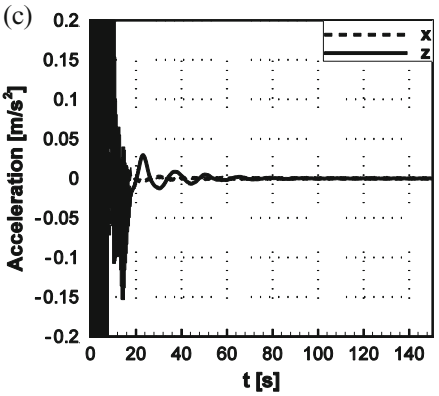

Acceleration of centre of gravity.

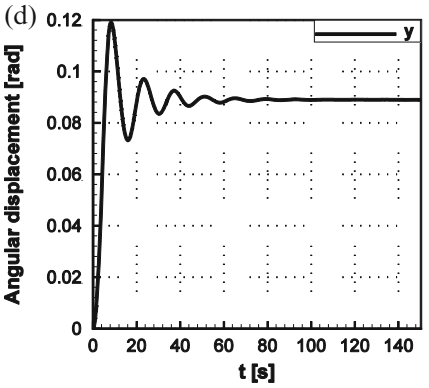

Angular displacement.

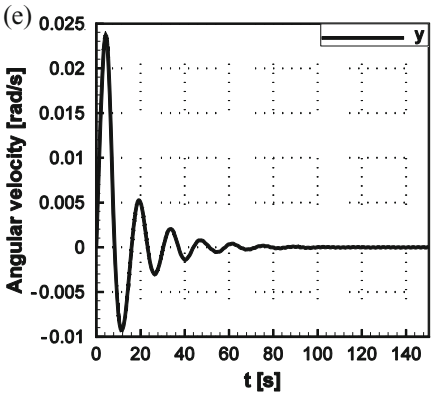

Angular velocity.

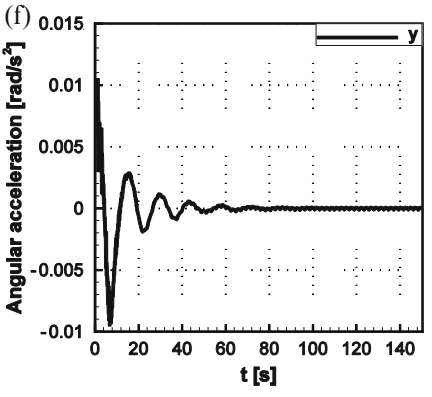

Angular acceleration.

Fig. 17.13 Lateral and rotational dynamics of the support for decoupled case

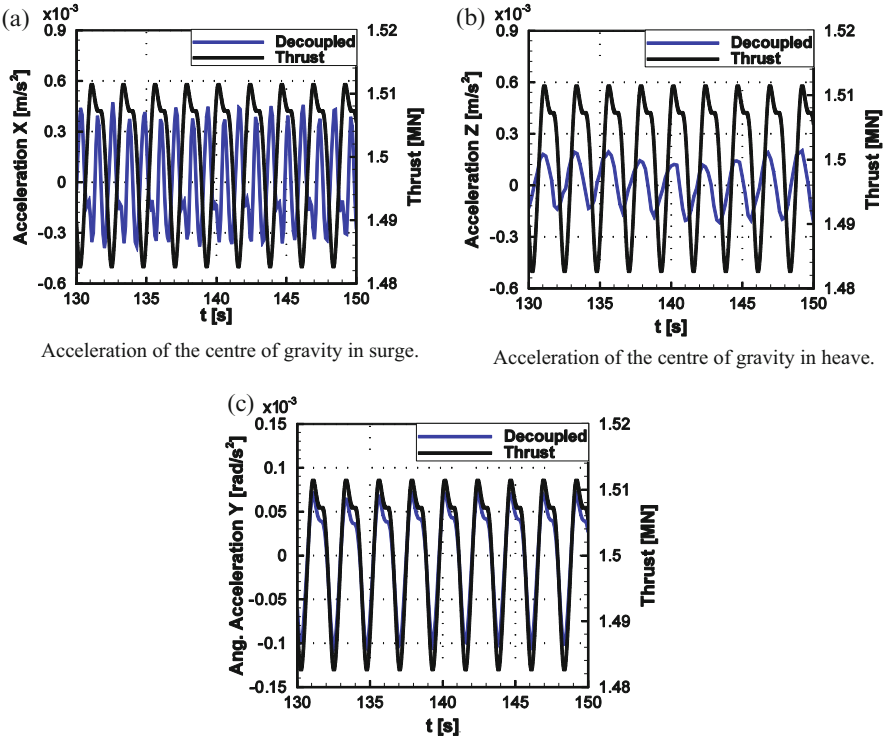

Acceleration of the centre of gravity in surge.

Acceleration of the centre of gravity in heave.

Pitching acceleration about the centre of gravity.

Fig. 17.14 The last 20 s of lateral and rotational accelerations of the support for decoupled case

results suggest otherwise, as shown in Fig. 17.15a. As can be seen, only the mooring lines are responsible for balancing the thrust force.

Since the water is considered calm for the decoupled case, the only source of hydrodynamic force acting in x direction is the hydrodynamic damping. Therefore, it is acting in the opposite direction of the motion, and as a result in opposite direction to the mooring force, which is a main source of motion in this direction. Lastly, small spurious moments and forces are noted, e.g. force in sway (y direction), which is normal to the plane of symmetry of the support. This is due to the SPH, where motion of the particles is never indeed symmetric. However, these discrepancies diminish with the number of particles, as was seen when test cases from Table 17.4 were computed.

Further, the SPH method is known for its pressure instabilities, where the pressure field of the particles exhibits large pressure oscillations due to acoustic waves present in compressible fluids. This is commonly tackled with solution smoothing techniques, also termed particles smoothing. Schemes up to the second order were proposed in the literature (Belytschko et al. 2000; Bilotta et al. 2011). In the present work, no particles smoothing was applied, including validation test

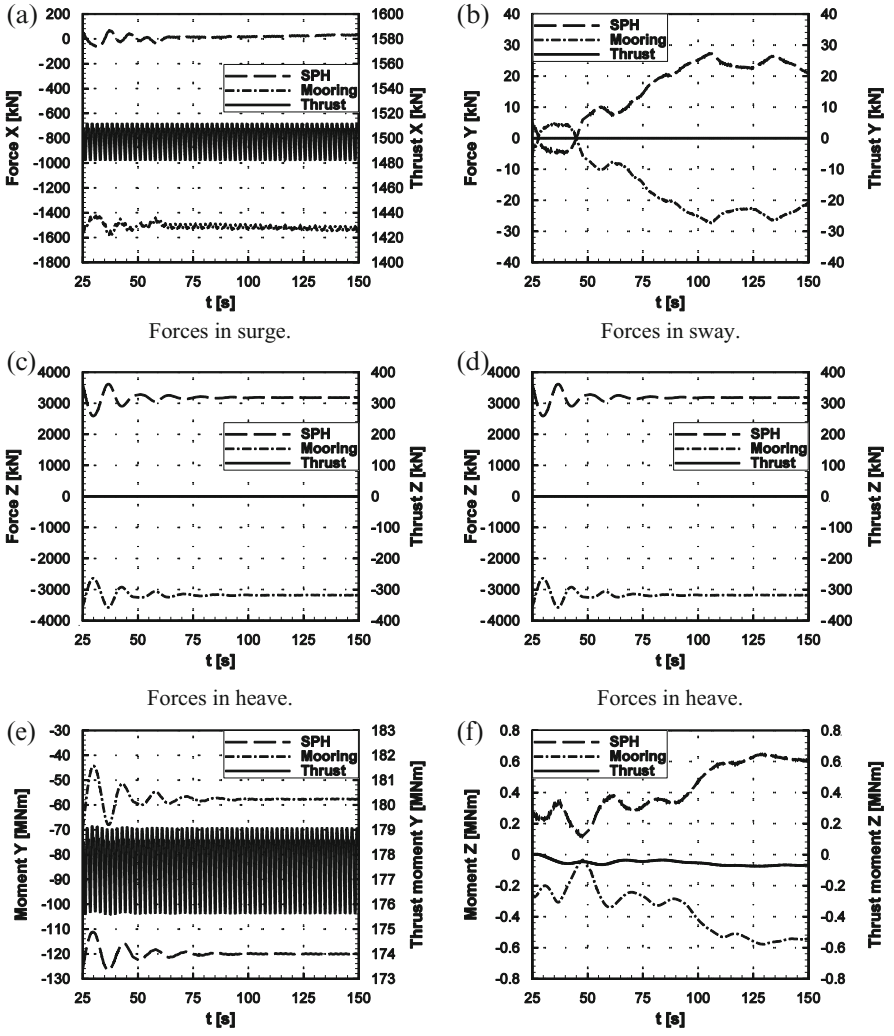

Fig. 17.15 Forces and moments acting at CoG of the support for decoupled case

cases. In fact, stability issues were encountered when a zero-order Shepard density filter was applied to the decoupled test case every 50 and 100 SPH steps. However, smoothing was shown to have a small effect on the overall pressure distribution for the artificial viscosity formulation used in this work (Gomez-Gesteira et al. 2012).

17.4.2 Coupled Case

Coupled computations were also performed, and results are presented in Fig. 17.16. As was mentioned in Sect. 17.2.5, the time step for SPH was set to $\Delta t_{SPH} = 2 \times 10^{-4}$ s, whereas HMB3 employed a time step of $\Delta t_{HMB3} = 2 \times 10^{-2}$ s $= 100 \Delta t_{SPH}$, or 1.06° of revolution per time step. The aerodynamic forces acting on the rotor as functions of time are shown in Fig. 17.17a. The platform motion shows similar trend as for the previous, decoupled test case. However, the rotor thrust is now dependent on the position and velocity of the rotor. As the wind turbine pitches under the thrust force, the rotor moves in the direction of the wind (velocity in x direction in Fig. 17.17b). In return, the thrust force decreases due to the reduced inflow speed and the orientation of the rotor disk. As the applied force is reduced, the rotor velocity decreases. The inverse relation between the aerodynamic force and velocity of the hub in x direction is clear in Fig. 17.17. Further, due to the pitch angle, a component of the thrust is acting along the z axis. As a result, the FOWT experiences higher displacement in heave: −0.8 m as compared to −0.6 m for the decoupled solutions. The initial motion of the FOWT is dominated by the imbalance of the forces due to the applied thrust, and the effect of the first wave passage is not visible. However, the effect of every consecutive wave is clearly visible in periodic variation of the moment about the y axis, as shown in Fig. 17.16f.

To facilitate the analysis of forces and moments acting on the system, the aerodynamic moments were transferred to the centre of gravity of the support platform. The resulting time histories of forces and moments for the coupled test case are presented in Fig. 17.18. First, we observe lasting for about 10 s high frequency hydrodynamic forces and moments due to initial particles settling. Similar was observed for decoupled test case. After an initial phase, the hydrodynamic forces show periodic variation related to the frequency of the passing waves. Next, the mooring line forces are opposing the SPH forces in all directions. Finally, periodic variation of the aerodynamic forces with frequency of the waves is noted. A phase shift is present, since the aerodynamic forces are dependent on velocity and position, rather than on forces, as was discussed in previous paragraphs.

For the moments, pitching moment (about y) is dominating and after the initial phase the solvers tend to a periodic solution. The aerodynamic moment follows the inverse relation to the hydrodynamic pitching moment. The phase shift for the mooring lines moment is present, as it depends on the orientation of the support. The aerodynamic moment about x axis applied at the rotor is a result of a driving force created by the lift and drag. Clearly, the driving force follows the same trend as the thrust force i.e. inverse relation with the velocity of the hub. The aerodynamic moment is transferred to the structure, and hydrodynamic and mooring lines moments are trying to compensate for this moment. Finally, the mooring lines are opposing the hydrodynamic moments for the moment about z axis (yawing).

Note that no significant gyroscopic effect was observed for this FOWT. The value of gyroscopic moment can be estimated using gyroscopic approximation as

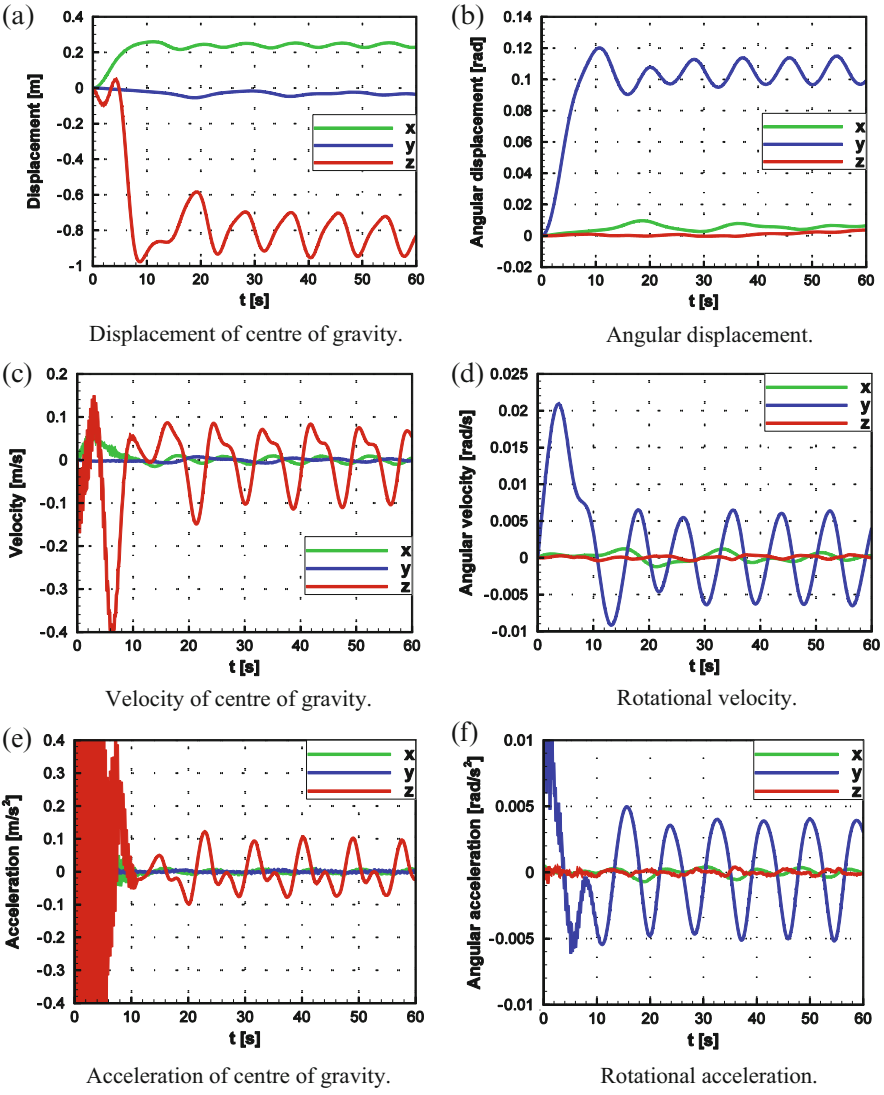

Fig. 17.16 Lateral and rotational dynamics of the support platform for coupled test case

$\tau = I_{zz}\omega_r\omega_p$. In this case the precession rate ω_p is caused by the waves, and gyroscopic torque τ should develop about body-fixed yaw axis. The pitching angular velocity is shown in Fig. 17.16d and follows sinusoidal shape with amplitude $\omega_p \approx 0.006$ rad/s. Given that the angular velocity of the rotor $\omega_r = 0.92$ rad/s $\gg \omega_p$, some of the gyroscopic approximation assumptions are still valid. Substituting the above values and the mass moment of inertia of the rotor from Table 17.3 into the

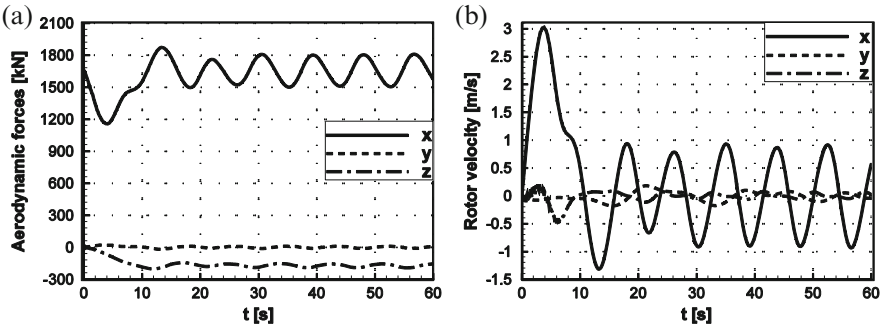

Aerodynamic forces acting on the rotor. Velocity of centre of gravity of the rotor.

Fig. 17.17 Forces acting on the rotor and velocity of centre of gravity of the rotor as function of time for coupled computation

equation of gyroscopic approximation, it follows that the amplitude of gyroscopic torque is $\tau = 0.86$ MNm.

Since FOWT is oscillating about a mean pitch angle of about 0.11 rad (6.3°), the gyroscopic torque has two components when projected on the direction of global axes: one about the global z-axis $\tau_z = 0.77$ MNm, and one about the global x-axis $\tau_x = 0.09$ MNm. As can be seen, the estimated magnitude of the rolling gyroscopic torque is about 0.75 % of the mean aerodynamic moment in roll. Therefore, it can be considered negligible. On the other hand, the gyroscopic torque in yaw is comparable to other moments about the z-axis. However, those small moments did not cause significant rotation of the FOWT about this axis due to large inertia of the floater. The estimated magnitude of the gyroscopic torque is about 0.35 % of the mean aerodynamic moment in pitch. This agrees with the observations made by Velazquez and Swartz (2012) that gyroscopic effect and resulting moment is small (less than 5 %) as compared to the pitching moment for horizontal axis wind turbines with low speed rotors.

Figure 17.19 presents different positions of the FOWT during the computation. The wave breaking effect of the support structure is visible, and the recovery of the waves behind the FOWT can be seen. The change of the pressure on the rotor can also be observed, especially at the tip of the nacelle. Note that the tower was not included in the aerodynamic domain; it is, however, shown in the figure, as the presence of the tower was accounted for in the multi-body model.

17.4.3 Computational Performance

For all cases, the SPH solver with MBDM were executed on a single 8 cores Intel® Xeon® CPU machine with 16 threads. Each of the CPU cores had a clock rate of 2 GHz, and 6.6 GB of dedicated memory. As no interconnect switch was

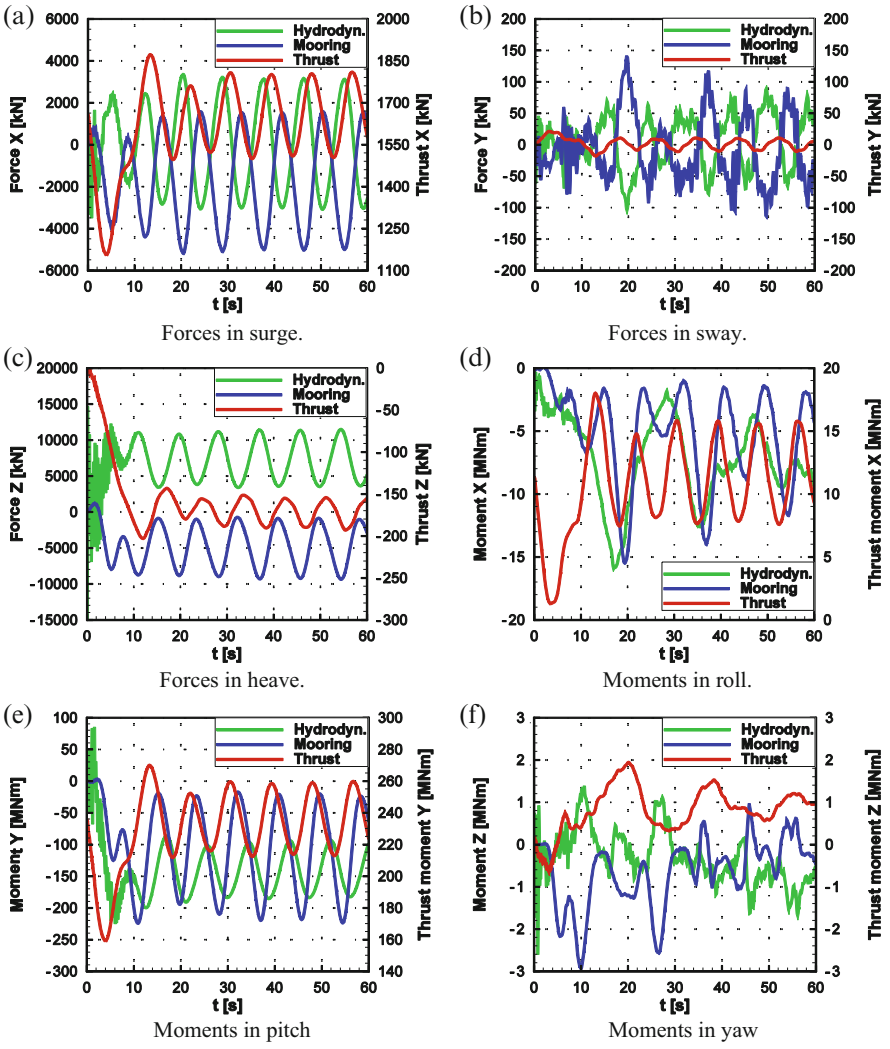

Fig. 17.18 Forces and moments acting at CoG of the support for the coupled test case

involved, the message passing delay between SPH and MBDM solvers was reduced to minimum. For the coupled case, HMB3 was executed on 29 dual-core AMD Opteron™ processors with 4 threads, giving in total 116 parallel instances of the solver. Each of the CPU cores had a clock rate of 2.4 GHz, and 4 GB of random access memory. It should be noted that the SPH method requires only local (limited by the kernel function) weighted average in the vicinity of the given particle, whereas HMB3 solves the complete set of equations involving all the cells in the

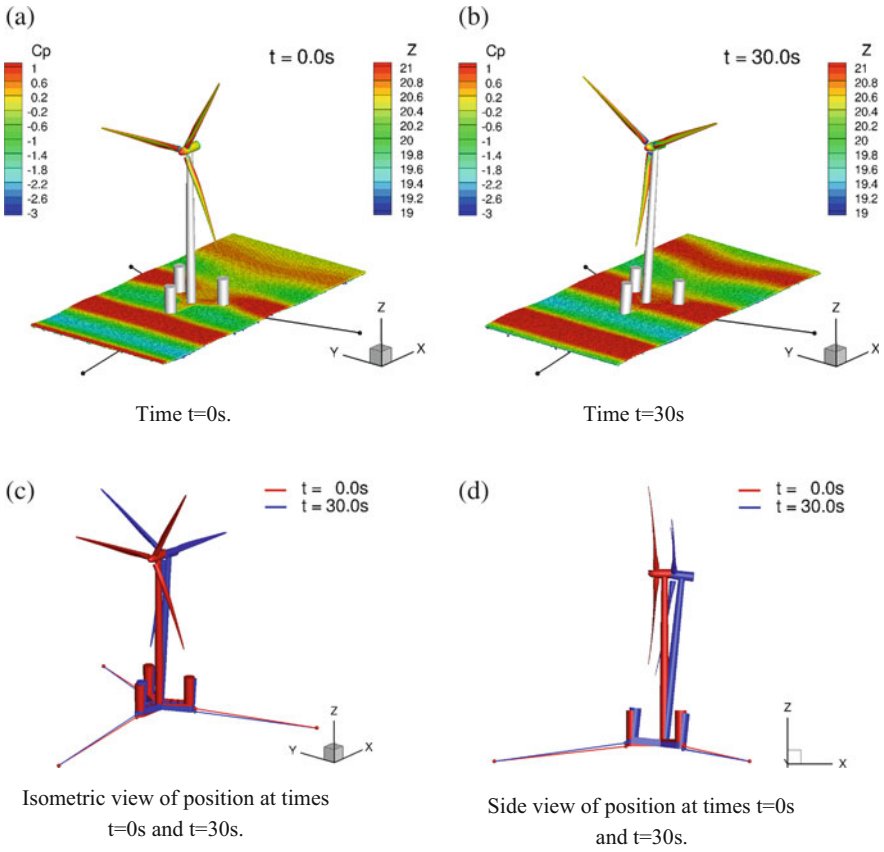

Fig. 17.19 Position and orientation of the FOWT at times $t = 0$ s and $t = 30$ s during coupled computation. Contours on the rotor correspond to pressure coefficient Cp, contours on the water surface correspond to surface elevation z in meters

domain. Hence, more processing units were assigned to the aerodynamic side of the coupled problem.

The average time required to compute a second of the solution for the coupled case is 27.26 h, where about 27.25 h were spent to solve aerodynamics, 21.3 h to solve hydrodynamics, and 0.24 h to solve multi-body equations. The average time spent to exchange information for a second of the solution is 0.53 s, and was mostly dictated by the communication between the SPH and the MBDM solvers.

It should be noted that time accuracy can be improved, if the coupling step is reduced. In the presented coupled case, the information is exchanged every 100 SPH steps ($\Delta t = 2 \times 10^{-2}$). When information between the solvers is exchanged every 50 SPH steps ($\Delta t = 1 \times 10^{-2}$), the average time required to compute a second of the solution becomes 45.0 h. If information is exchanged every single SPH step ($\Delta t = 2 \times 10^{-4}$), the average time per one second extends to about 438.9 h.

Table 17.5 Computational performance of the coupling algorithm for various coupling time steps

Coupling Δt (s)	HMB3 CFL no.	HMB3 Newton steps	SPH steps	Time per coupling step (s)	Time per 1s of solution (s)
2×10^{-2}	5.0	315	100	1.95×10^{3}	9.81×10^{4}
2×10^{-2}	10.0	350	100	2.29×10^{3}	1.15×10^{5}
1×10^{-2}	5.0	237	50	1.61×10^{3}	1.62×10^{5}
1×10^{-2}	10.0	105	50	1.04×10^{3}	1.06×10^{5}
2×10^{-4}	5.0	45	1	3.13×10^{2}	1.58×10^{6}
2×10^{-4}	10.0	23	1	1.59×10^{2}	7.97×10^{5}

In the former case, HMB3 requires on average 237 pseudo-time steps to achieve the level of convergence below 10^{-2}, and 45 pseudo-time steps for the latter case. The convergence is defined as L2-norm of the residual vector. This suggests that computational cost can be further reduced by employing explicit schemes for both solvers and performing less evaluations (four for Runge-Kutta scheme of 4th order). However, the biggest possible explicit step for HMB3 that would satisfy explicit CFL condition of 0.4 for the smallest cell in the domain is about 3.6×10^{-9} s. Therefore, the aerodynamic time-step becomes the limiting factor for this approach and for the problem at hand. More information about the computational performance is presented in Table 17.5. Stability issues were encountered for a time step $\Delta t = 2 \times 10^{-2}$ and HMB3 implicit CFL number 10.0, where the residual vector does not converge as fast as for CFL number 5.0. This indicates that CFL number of about 8.0 would be an optimal choice for this time step.

17.5 Conclusions

The chapter presented a coupling method for the analysis of the dynamics of floating offshore wind turbines. The HMB3 CFD solver was used for the analysis of blade aerodynamics and via a multi-body dynamics method it was coupled to a smoothed particle hydrodynamics tool to model the floating part of the turbine. The results showed that the weak coupling method is adequate for the solution of the problem at hand. Due to the lack of experimental data for a coupled system, validation was only possible for the components of the model. Data from the MEXICO project were used for aerodynamics; good overall agreement has been seen between CFD and test data. For the hydrodynamics solver, experiments related to drops of solid objects in water were used. Again, with a refined set of particles, the SPH method delivered good results. The third component of the method was the multi-body dynamics and this was validated using simple slider-crank problems.

Presented results demonstrated that a FOWT is a highly dynamic system. To obtain a deeper understanding of how rotor thrust and torque vary under dynamic conditions, efforts should be put forward to study the aerodynamic flow and loads as a wind turbine undergoes prescribed motion in pitch and yaw. It should be noted

that the spatial resolution of water employed in this work can be improved. In the future, a finer set of SPH particles will be employed and the tower will be included in the aerodynamic domain. Also, in the future, the work will continue with the validation of the method against experimental data, when available, and comparisons with a strong coupling technique. Another aspect that should be addressed is the experimental measurements. Clearly, each of the components can be validated separately, but the set of comprehensive data for the complete FOWT system is crucial for the model validation. The following measurements would be an asset: forces and moments due to the mooring system, water basin tests with small- or full-scale wind turbine including pressure distributions on support and rotor, and the overall FOWT time response including transient and periodic states.

Acknowledgments Results were obtained using the EPSRC funded ARCHIE-WeSt High Performance Computer (www.archie-west.ac.uk). EPSRC grant no. EP/K000586/1.

References

Arapogianni A, Genachte AB, Ochagavia RM et al (2013) Deep water – the next step for offshore wind energy. In: European Wind Energy Association Publications. Available via EWEA. http://www.ewea.org/fileadmin/files/library/publications/reports/Deep_Water.pdf. Accessed 11 Apr 2016

Axelsson O (1994) Iterative solution methods. Cambridge University Press, Cambridge

Bak C, Zahle F, Bitsche R et al (2013) The DTU 10-MW reference wind turbine. In: DTU orbit – the research information system. Available via Technical University of Den-mark. http://orbit.dtu.dk/files/55645274/The_DTU_10MW_Reference_Turbine_Christian_Bak.pdf. Accessed 06 Apr 2016

Barakos G, Steijl R, Badcock K et al (2005) Development of CFD capability for full helicopter engineering analysis. In: Abstracts of the 31st European Rotorcraft Forum 2005, AIDAA, Florence, 13–15 September 2005

Belytschko T, Guo Y, Kam Liu W et al (2000) A unified stability analysis of meshless particle methods. Int J Numer Methods Eng 48(9):1359–1400

Benitz M, Schmidt D, Lackner M et al (2015) Validation of hydrodynamic load models using CFD for the OC4 – DeepCwind Semisubmersible. Paper presented at the 33rd international conference on ocean, offshore and arctic engineering, ASME, St. John's, May 31–June 5 2015

Beyer F, Arnold M, Cheng PW (2013) Analysis of floating offshore wind turbine hydrodynamics using coupled CFD and multibody methods. In: Chung JS, Langen I, Kokkinis T et al (eds) Proceedings of the twenty-third (2015) international offshore and polar engineering conference, Anchorage, June–July 2013. ISOPE, California, p 261

Bilotta G, Russo G, Herault A et al (2011) Moving least-squares corrections for smoothed particle hydrodynamics. Ann Geophys. doi:10.4401/ag-5344

Björck (1990) Coordinates and calculations for the FFA-W1-xxx, FFA-W2-xxx and FFA-W3-xxx series of airfoils for horizontal axis wind turbines. Technical report, The Aeronautical Research Institute of Sweden. In: National Renewable Energy Laboratory documents. Available via National Wind Technology Center's Information Portal (NWTC). https://wind.nrel.gov/airfoils/Documents/FFA%20TN%201990-15%20v.1-2%20c.1.pdf. Accessed 11 Apr 2016

Carrión M, Woodgate M, Steijl R et al (2013) Implementation of all-mach roe-type schemes in fully implicit CFD solvers – demonstration for wind turbine flows. Int J Numer Methods Fluids 73(8):693–728. doi:10.1002/fld.3818

Carrión M, Steijl R, Woodgate M et al (2014a) Aeroelastic analysis of wind turbines using a tightly coupled CFD-CSD method. J Fluid Struct 50:392–415

Carrión M, Steijl R, Woodgate M et al (2014b) Computational fluid dynamics analysis of the wake behind the MEXICO rotor in axial flow conditions. Wind Energy 18(6):1023–1045. doi:10.1002/we.1745

Carrión M, Woodgate M, Steijl R et al (2015) Understanding wind-turbine wake breakdown using computational fluid dynamics. AIAA J 53(3):588–602

Castain R, Ladd J, Solt D et al (2015) Supercomputing 2015 PMIx BoF slides. In: Open MPI super computing papers. Available via Open MPI. https://www.open-mpi.org/papers/sc-2015-pmix/PMIx-BoF.pdf. Accessed 11 Apr 2016

Degroote J, Haelterman R, Annerel S et al (2010) Performance of partitioned procedures in fluid-structure interaction. Comput Struct 88(7-8):446–457

Dehaeze F, Barakos GN (2012a) Hovering rotor computations using an aeroelastic blade model. Aeronaut J 116(1180):621–650

Dehaeze F, Barakos GN (2012b) Mesh deformation method for rotor flows. J Aircraft 49(1):82–92. doi:10.2514/1.C031251

Eisenstat SC, Elman HC, Schultz MH (1983) Variational iterative methods for nonsymmetric systems of linear equations. SIAM J Numer Anal 20(2):345–357. doi:10.1137/0720023

Farhat C, Van der Zee K, Geuzaine R (2006) Provably second-order time-accurate loosely-coupled solution algorithms for transient nonlinear computational aeroelasticity. Comput Methods Appl Mech 195:1973–2001

Fellipa CA, Park KC, Farhat C (1999) Partitioned analysis of coupled mechanical systems: Technical Report CU-CAS-99-06. In: University of Colorado, Department of Aerospace Engineering Sciences, Center for Aerospace Structures (CAS), Publications. Available via CAS. http://www.colorado.edu/engineering/CAS/Felippa.d/FelippaHome.d/Publications.d/Report.CU-CAS-99-06.pdf. Accessed 11 Apr 2016

Fernández MA, Moubachir M (2005) A newton method using exact Jacobians for solving fluid-structure coupling. Comput Struct 83:127–142. doi:10.1016/j.compstruc.2004.04.021

Gomez-Gesteira M, Rogers BD, Crespo AJ et al (2012) SPHysics – development of a free-surface fluid solver – part 1: theory and formulations. Comput Geosci 48:289–299. doi:10.1016/j.cageo.2012.02.029

Gómez-Iradi S, Steijl R, Barakos GN (2009) Development and validation of a CFD technique for the aerodynamic analysis of HAWT. J Sol Energy Eng. doi:10.1115/1.3139144

Greenhow M, Lin WM (1983) Nonlinear-free surface effects: experiments and theory. Technical Report 83–19, Massachusetts Institute of Technology, Department of Ocean Engineering. In: US Department of Defense publications. Available via Defense Technical Information Center (DTIC). http://www.dtic.mil/dtic/tr/fulltext/u2/a161079.pdf. Accessed 11 Apr 2016

Jameson A (1991) Time dependent calculations using multigrid, with applications to unsteady flows past airfoils and wings. In: Abstracts of the 10th computational fluid dynamics conference, fluid dynamics and co-located conferences, AIAA, Honululu, 24–26 June 1991

Jarkowski M, Woodgate MA, Barakos GN et al (2013) Towards consistent hybrid overset mesh methods for rotorcraft CFD. Int J Numer Methods Fluids 74(8):543–576. doi:10.1002/fld.3861

Jonkman J (2007) Dynamics modeling and loads analysis of an offshore floating wind turbine, technical report NREL/TP-500-41958. In: National Renewable Energy Laboratory Documents. Available via NREL. http://www.nrel.gov/docs/fy08osti/41958.pdf. Accessed 11 Apr 2016

Karimirad M, Moan T (2012) A simplified method for coupled analysis of floating offshore wind turbines. Mar Struct 27(1):5–63

Karimirad M, Moan T (2013) Modeling aspects of a floating wind turbine for coupled wave – wind-induced dynamic analyses. Renew Energ 53:299–305

Küttler U, Wall WA (2008) Fixed-point fluid–structure interaction solvers with dynamic relaxation. Comput Mech 43(1):61–72

Larsen TJ, Hanson TD (2007) A method to avoid negative damped low frequent tower vibrations for a floating, pitch controlled wind turbine. J Phys Conf Ser. doi:10.1088/1742-6596/75/1/012073

Leble V, Barakos G (2016) Demonstration of a coupled floating offshore wind turbine analysis with high-fidelity methods. J Fluid Struct 62:272–293

Lee WT, Bales SL, Sowby SE (1985) Standardized wind and wave environments for North Pacific Ocean Areas. David W Taylor Naval Ship Research and Development Center. Technical Report DTNSRDC/SPD-0919-02. In: US Department of Defense publications. Available via Defense Technical Information Center (DTIC). http://www.dtic.mil/cgi-bin/GetTRDoc?Location=U2&doc=GetTRDoc.pdf&AD=ADA159393. Accessed 11 Apr 2016

Leimkuhler BJ, Reich S, Skeel RD et al (1996) Integration methods for molecular dynamics springer. In: Schulten K, Sumners DW (eds) Mathematical approaches to biomolecular structure and dynamics. The IMA volumes in mathematics and its applications, vol 82. Springer, New York, p 161

Marino E, Borri C, Peil U (2011) A fully nonlinear wave model to account for breaking wave impact loads on offshore wind turbines. J Wind Eng Ind Aerod 99(4):483–490

Matha D, Schlipf M, Cordle A et al (2011) Challenges in simulation of aerodynamics, hydrodynamics, and mooring-line dynamics of floating offshore wind turbines. Paper presented at the 21st offshore and polar engineering conference, Maui, 19–24 June 2011

Morison J, O'Brein M, Johnson J et al (1950) The force exerted by surface waves on piles. J Petrol Technol 2:149–154

Nikravesh PE (1988) Computer-aided analysis of mechanical systems. Prentice Hall, Upper Saddle River

Osher S, Chakravarthy S (1983) Upwind schemes and boundary conditions with applications to Euler equations in general geometries. J Comput Phys 50(3):447–481

Rieper F (2011) A low-Mach number fix for Roe's approximate Riemann solver. J Comput Phys 230(13):5263–5287. doi:10.1016/j.jcp.2011.03.025

Roald L, Jonkman J, Robertson A et al (2013) The effect of second-order hydrodynamics on floating offshore wind turbines. Energy Procedia 35:253–264

Roddier D, Cermelli C, Weinstein A (2009) WindFloat: a floating foundation for offshore wind turbines – part I: design basis and qualification process. In: Abstracts of the ASME 2009 28th international conference on ocean, offshore and arctic engineering, ASME, Honolulu, 31 May–5 June 2009

Savenije LB, Ashuri T, Bussel GJ et al (2010) Dynamic modeling of a spar-type floating offshore wind turbine. Paper presented at the European Wind Energy Conference and Exhibition (EWEC), Warsaw, 20–23 April 2010

Schepers JG, Snel H (2007) Model experiments in controlled conditions, final report ECN-E–07-042. In: Energy Research Center of the Netherlands (ECN) reports. Available via ECN. http://www.ecn.nl/docs/library/report/2007/e07042.pdf. Accessed 11 Apr 2016

Schepers JG, Snel H (2012). Final report of IEA Task 29, MexNext (Phase I): analysis of Mexico wind tunnel measurements. Technical Report, Energy Research Center of the Netherlands, ECN. In: Energy Research Center of the Netherlands (ECN) reports. Available via ECN. http://www.mexnext.org/fileadmin/mexnext/user/documents/FinRep_Mexnext_v6_opt.pdf. Accessed 11 Apr 2016

Skaare B, Hanson T, Nielsen F et al (2007) Integrated dynamic analysis of floating offshore wind turbines. Paper presented at the European Wind Energy Conference and Exhibition (EWEC), Milan, 07–10 May 2007

Spalart P, Jou W, Strelets M et al (1997) Comments on the feasibility of LES for wings, and on a hybrid RANS/LES approach. In: Liu C, Liu Z (eds) Proceedings of the first AFOSR international conference on DNS/LES, Louisiana, 1997

Steijl R, Barakos G (2008) Sliding mesh algorithm for CFD analysis of helicopter rotor-fuselage aerodynamics. Int J Numer Methods Fluids 58:527–549. doi:10.1002/fld.1757

Velazquez A, Swartz RA (2012) Gyroscopic effects of horizontal axis wind turbines using stochastic aeroelasticity via spinning finite elements. In: Abstracts of the ASME 2012 conference on smart materials, adaptive structures and intelligent systems, ASME, Stone Mountain, 19–21 September 2012

Vierendeels J, Lanoye L, Degroote J et al (2007) Implicit coupling of partitioned fluid-structure interaction problems with reduced order models. Compos Struct 85:970–976. doi:10.1016/j.compstruc.2006.11.006

Woodgate MA, Barakos GN, Scrase N et al (2013) Simulation of helicopter ditching using smoothed particle hydrodynamics. In: Abstracts of the 39th European Rotorcraft Forum 2013. AIDAA, Moscow, 3–6 September 2013

Zienkiewicz O, Taylor R, Zhu JZ (2005) The Finite element method, 6th edn. Butterworth-Heinemann, Oxford

Chapter 18
CFD Study of DTU 10 MW RWT Aeroelasticity and Rotor-Tower Interactions

Sergio González Horcas, François Debrabandere, Benoît Tartinville, Charles Hirsch, and Grégory Coussement

Abstract A numerical analysis of the DTU 10 MW RWT wind turbine aerodynamics is presented in this work. The development of an innovative methodology based on three-dimensional computational fluid dynamics allowed to tackle two challenging problems related to this application. On one hand, the impact of blade deflections on rotor performance was assessed in a *rotor-only* context. Different blade configurations were studied, including the installation of *Gurney flaps* and the consideration of *prebending* and *preconing*. On the other hand, flow unsteadiness of the *full machine* (i.e. including the tower) was modeled by means of the *Non-Linear Harmonic* method. This approach allowed to characterize local aspects of the flow and the impact of *rotor-tower interactions* on the computed loads.

18.1 Introduction

Industry standards for the aeroelastic simulations of horizontal axis wind turbines are based on the *Blade Element Momentum* (BEM) theory. For classical machine designs, such a method offers a very good computational efficiency and an acceptable flow response. BEM base formulation has been improved along with *onshore* wind turbines evolution, thanks to the introduction of additional sub-models (Jonkman and Buhl 2007; Heege et al. 2013). The accuracy of this approach is however limited when dealing with large *Offshore Wind Turbine* (OWT) rotors due to the existence of highly skewed flows and heavy detachments. Hence, the use of more sophisticated *Computational Fluid Dynamics* (CFD) techniques is justified.

S.G. Horcas (✉) • F. Debrabandere • B. Tartinville • C. Hirsch
NUMECA International, 189 Ch. de la Hulpe, B-1170 Bruxelles, Belgium
e-mail: sergio.horcas@gmail.com; francois.debrabandere@numeca.be; benoit.tartinville@numeca.be; charles.hirsch@numeca.be

G. Coussement
Faculty of Engineering, Fluids-Machines Department, University of Mons, 53 Rue du Joncquois, B-7000 Mons, Belgium
e-mail: gregory.coussement@umons.ac.be

W. Ostachowicz et al. (eds.), *MARE-WINT*, DOI 10.1007/978-3-319-39095-6_18

Due to the continuous upscaling of modern OWTs, important *aeroelastic effects* are also expected. Traditional CFD approaches do not consider the flexibility of the rotor. However, blade deflections can have a non negligible impact on the machine performance, and a possible *blade-tower impact* should be considered at the design stage. This requires the consideration of rotor structural models in CFD computations. Due to the lack of publicly available *industrial* configurations, previous studies concerning wind turbines *aeroelasticity* are based on the so-called *academic* or *reference* designs. In this group we find the works of Corson et al. (2012) for the SNL-100-00 blade and the studies of the NREL 5 MW performed by Hsu and Bazilevs (2012) and Yu and Kwon (2014). In all these publications, blade deflections were found to have a direct impact on the final rotor performance.

Previous CFD studies of wind turbine rotors are based on steady flow *rotor-only* simulations (where only blades, hub and nacelle geometries are considered). Thanks to the problem periodicity when assuming an incoming wind aligned with the rotor axis, a single *blade passage* is normally meshed. These simulations allow to characterize the local flow behaviour around the wind turbine and its impact on global rotor performance with a reduced computational effort. However, by omitting the tower geometry the main source of flow unsteadiness is also neglected. Indeed, due to the proximity of the rotor to the tower, the generation of complex unsteady flow phenomena is expected. This mechanism is often referred as *rotor-tower interactions*. First NREL Phase VI publications assessing this topic revealed the existence of both blade and tower *shedding* phenomena and fluctuating loads generation related to the *blade-tower alignment* event (Zahle et al. 2009; Lynch 2011; Wang et al. 2012; Hsu et al. 2014; Li 2014). Similar unsteady effects were computed for the NREL 5 MW studies of Hsu and Bazilevs (2012) and Yu and Kwon (2014), and in the *industrial* wind turbines publications of Zahle and Sørensen (2008, 2011).

In this chapter high fidelity CFD models were used in order to characterize the rotor aerodynamics of the DTU 10 MW RWT *reference* wind turbine (Bak et al. 2013), whose main parameters are summarized in Table 18.1. *Aeroelasticity* and *rotor-tower interactions* problems were assessed in two independent numerical studies. In Sect. 18.2, *rotor-only* simulations were performed based on the computational framework for OWT rotors *static aeroelasticity* analysis developed by Horcas et al. (2014). In particular, the impact of *Gurney flaps* installation and the effect of *prebending* and *preconing* on rotor performance were evaluated. This work can be understood as a continuation of previous DTU 10 MW RWT studies (Horcas et al. 2015a,b). In Sect. 18.3, the flow unsteadiness related to *rotor-tower interactions* was characterized by means of the *Non Linear Harmonics* (NLH) method presented by Vilmin et al. (2006).

The present computational analysis was performed using the commercial CFD package FINE™/Turbo (NUMECA International 2013b). This tool was previously validated in the framework of NREL Phase VI *rotor-only* simulations by other authors (Fan and Kang 2009; Elfarra et al. 2014; Suárez et al. 2015a,b). The FINE™/Turbo solver is a three-dimensional, density-based, structured, multi-

Table 18.1 DTU 10 MW RWT main parameters

Parameter description	Parameter value
Cut in wind speed	4 m s^{-1}
Cut out wind speed	25 m s^{-1}
Rated wind speed	11.4 m s^{-1}
Rated power	10 MW
Number of blades	3
Rotor diameter	178.3 m
Min. rotor speed	6 RPM
Max. rotor speed	9.6 RPM
Hub height	119 m
Tower diameter top	5.5 m
Tower diameter base	8.3 m
Tower clearance	18.26 m

block finite volume code. A central-difference scheme is employed for the spatial discretization with Jameson type artificial dissipation. A four-stage explicit Runge-Kutta scheme is applied for the temporal discretization. Multi-grid method, local time-stepping and implicit residual smoothing are used in order to speed-up the convergence.

18.2 DTU 10 MW RWT Rotor-Only Analysis

In this section, a complete characterization of DTU 10 MW RWT aeroelasticity in a *rotor-only* framework is presented. A *Reynolds Averaged Navier Stokes* (RANS) approach was used in order to perform steady flow simulations of this OWT. Turbulence was considered by means of the Spalart–Allmaras model (Spalart and Allmaras 1992). Rotor was considered either as *rigid* or *flexible*. For the latter case, the consideration of a blade structure sub-model was necessary. Mesh deformation was carried out by the 3-steps *hybrid method* described in Horcas et al. (2015a).

First computations included in Sect. 18.2.1 were based on the standard DTU 10 MW RWT rotor, assuming a *rigid* configuration. *Straight* blades were considered, equipped with the so-called *Gurney flaps* devices at low span range [20 %, 30 %] (see Fig. 18.1). Obtained results were compared with three-dimensional CFD simulations performed by other authors. The same methodology was used in Sect. 18.2.2 to compare the performance of this standard blade with a *clean* variant, where the *Gurney flaps* were removed. Both *rigid* and *flexible* rotor configurations were studied. Finally, in Sect. 18.2.3 the impact of of *prebending* and *preconing* on DTU 10 MW RWT aeroelastic behaviour is assessed.

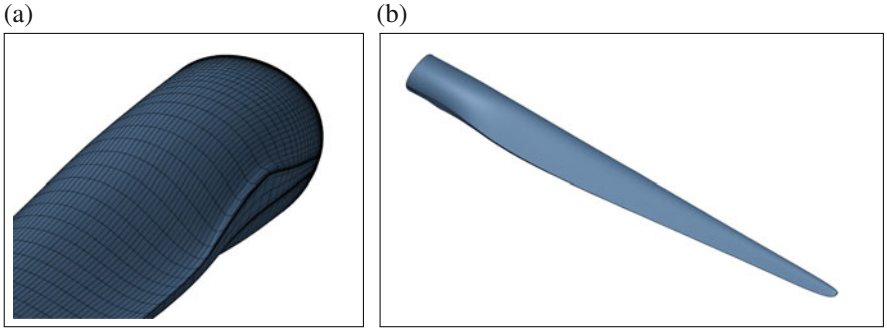

Fig. 18.1 DTU 10 MW RWT *straight* blade geometry equipped with *Gurney flaps*. (**a**) Low span zoom. (**b**) Global view

Table 18.2 DTU 10 MW RWT aerodynamic load cases definition

DLC Identifier	Wind speed [ms^{-1}]	RPM
FT_WSP07	7	6.000
FT_WSP08	8	6.426
FT_WSP09	9	7.229
FT_WSP10	10	8.032
FT_WSP11[a]	11	8.836

[a] FT_WSP11 being very close to the wind turbine design point, it is referred in this document as *rated speed*

18.2.1 Steady Aerodynamics, Standard Geometry

In this section, the DTU 10 MW RWT standard rotor was studied for the 0° pitch operating range compiled in Table 18.2. The hypothesis of *rigid* blades was made.

Autogrid5™ structured grids generator was used in order to perform a three-dimensional mesh of the DTU 10 MW RWT rotor (NUMECA International 2013a). Blade surfaces as well as original nacelle and hub geometries were included in this process. A blocking topology was established around the blade, putting special attention in the local mesh around the blunt edge and blade tip. A single blade passage was meshed, accounting for 7.2×10^6 nodes and 24 blocks. A first cell size of 3.0×10^{-5} m was imposed around the considered geometry, in order to properly describe the boundary layer for the studied wind speed range. Flow inlet and outlet were located at 2.2 and 3.2 blade radius from the nacelle respectively. Figure 18.2 shows a global overview of the mesh. For clarity purposes the three blades are displayed, and 1 out of 2 grid lines are skipped. In Fig. 18.3a, the cross-section mesh at mid-span is illustrated. The geometry of *Gurney flaps* at 20 % of span together with the surrounding cross-section mesh are shown in Fig. 18.3b.

A good agreement in terms of loads prediction with respect to the three-dimensional RANS computations described in Bak et al. (2013) and performed with

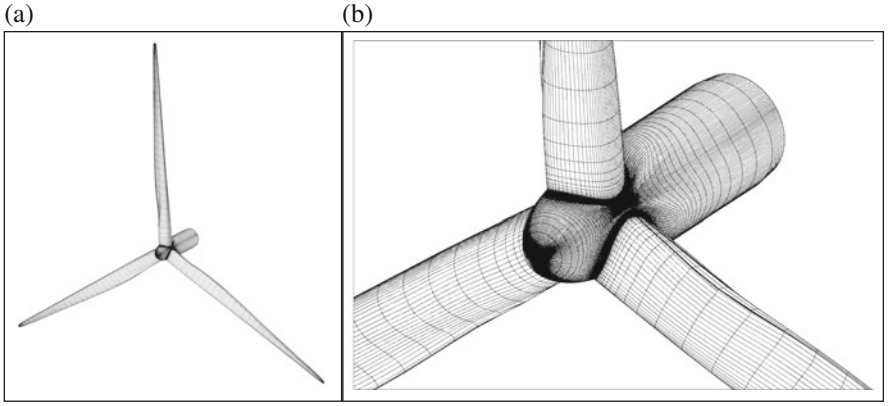

Fig. 18.2 DTU 10 MW RWT surface mesh overview (displayed 1 every 2 grid lines). (**a**) Global view. (**b**) Detail of nacelle and low blade span range

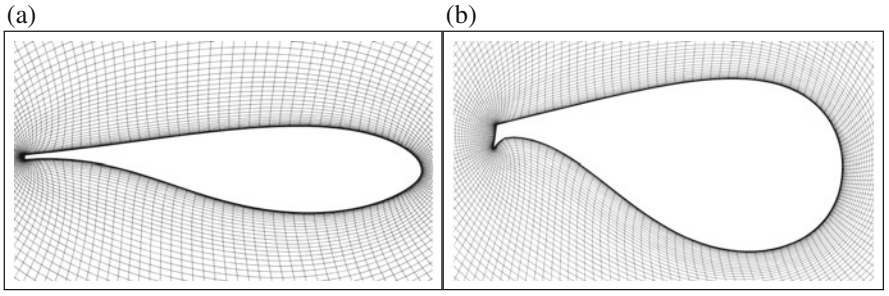

Fig. 18.3 DTU 10 MW RWT cross-section meshes, 20 and 50 % span. (**a**) 50 % span. (**b**) 20 % span

EllipSys3D (Sørensen 1995) was observed. A global loads comparison for all the studied operating points is included in Fig. 18.4.

Recirculations were observed near blade trailing edges at low span range. To illustrate this issue, Fig. 18.5 shows the friction streamlines around the DTU 10 MW RWT for the *rated speed* operating point. This observation is in-line with EllipSys3D computations performed by Zahle et al. (2014), where an important 3D flow behaviour was found up to an approximated radius of 30 m.

18.2.2 Static Aeroelasticity, Impact of Gurney Flaps

Original DTU 10 MW RWT blade geometry is equipped with the so-called *Gurney flaps* at low span range [20 %, 30 %]. This device, originally developed for race car applications, consists on a small plate located at the trailing edge. It is used to

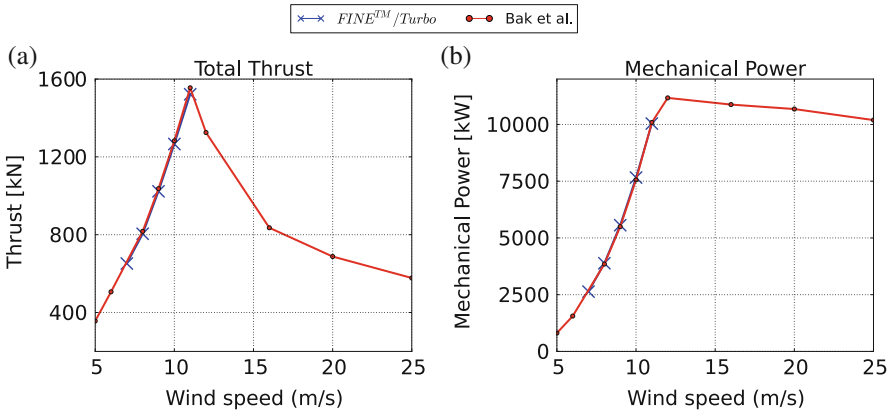

Fig. 18.4 DTU 10 MW RWT total rotor thrust and mechanical power versus wind speed. (**a**) Total thrust. (**b**) Mechanical power

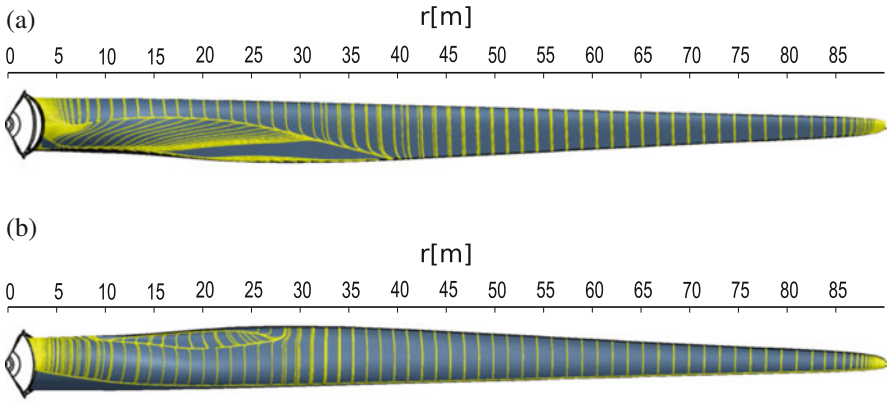

Fig. 18.5 Friction streamlines at *rated speed*. (**a**) Suction surface. (**b**) Pressure surface

increase the lift produced by the airfoil when operating in separated flow conditions. A low drag penalty is expected. First studies characterizing the performance of this passive device were performed by Liebeck (1978). Figure 18.6 reproduces the conclusions of this work. The beneficial effects of the *Gurney flaps* installation are explained by the re-attachment of suction side flow close to the trailing edge. In order to evaluate the behaviour of the DTU 10 MW RWT *Gurney flaps* the load cases of Table 18.2 were studied again in a mesh with *clean trailing edges*, and compared with previous results. This comparison was performed not only under the hypothesis of *rigid* blades, but also by considering a *flexible* rotor.

A new mesh was generated with the same set-up described in Sect. 18.2.1, but based on a variant geometry of the DTU 10 MW RWT where the *Gurney flaps* were replaced by the unmodified blade profiles definition. This new mesh is referred in

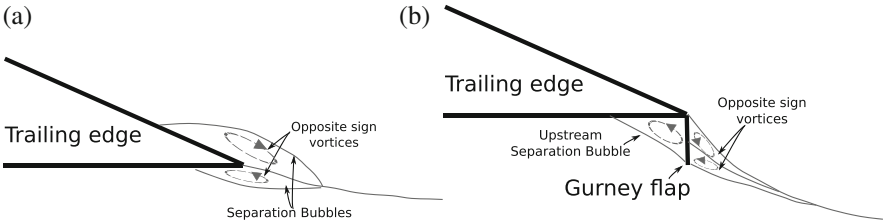

Fig. 18.6 Expected effects on trailing edge flow due to *Gurney flaps* installation. (**a**) Clean trailing edge. (**b**) Trailing edge accounting for a *Gurney flap*

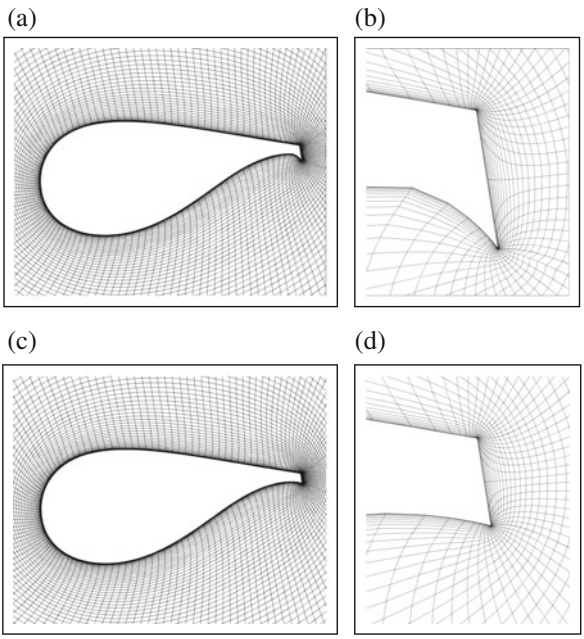

Fig. 18.7 Cross-section meshes at 25 % span for *G* (*Gurney*) and *NG* (*no-Gurney*) configurations. (**a**) *G* cross-section mesh. (**b**) *G* trailing edge. (**c**) *NG* cross-section mesh. (**d**) *NG* trailing edge

this section as *no-Gurney*, or *NG*. For clarity purposes, the one initially created in Sect. 18.2.1 is referred as *Gurney* or *G*. In order to illustrate the differences between *G* and *NG* configurations, Fig. 18.7 displays a cross-section of the mesh corresponding to a 25 % of blade span.

For the considered aeroelastic simulations, the blade structure was linearized by means of the *Reduced-Order Model* (ROM) developed by Debrabandere (2014). A modal analysis was performed within the commercial package Abaqus (Simulia 2008) based on the model provided by Bak et al. (2013). Obtained natural frequencies were compared against the results of the aeroelastic computations of HAWC2 (Larsen and Hansen 2007), a third party software based on *blade element*

Table 18.3 DTU 10 MW RWT blade modes, comparison in the absence of rotation

Natural frequency [Hz]		Isolated blade modes	
Abaqus	Bak et al. (2013)	Identifier	Description
0.61	0.61	1	1st flap
0.96	0.93	2	1st edge
1.75	1.74	3	2nd flap
2.88	2.76	4	2nd edge
3.58	3.57	5	3rd flap
5.71	5.69	6	1st torsion
5.75	–	7	Mixed flap/torsion
6.16	6.11	8	4th flap
–	6.66	9	3rd edge

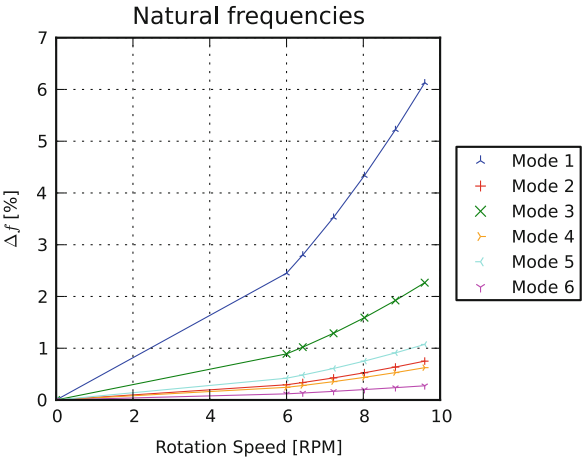

Fig. 18.8 Evolution of DTU 10 MW RWT blade frequencies in function of rotational speed (first six modes plotted)

momentum (BEM) theory. Computed frequencies for each identified mode are compiled in Table 18.3. To reduce the computational cost attached to aeroelastic simulations, only the first six frequencies of the obtained modal basis were used to model blade flexibility. A mixed mode was found between first torsion and fourth flap. No pure third edge mode was identified within the considered frequency range. These differences could be explained by the complexity of the astructural models used for natural frequencies extraction.

Additional modal analysis were performed taking into account the *centrifugal effects* of each one of the analyzed rotor RPMs. This allowed to include the *initial blade deformation* due to the rotation. In addition, a slight structural frequencies shift was observed. This effect is illustrated in Fig. 18.8, where the variations of blade frequencies against non-rotating frequency are plotted at every RPM. Even if this frequency shifting is not as important as in other rotatory applications including large blade deformations (such as helicopters), a non-negligible value is observed

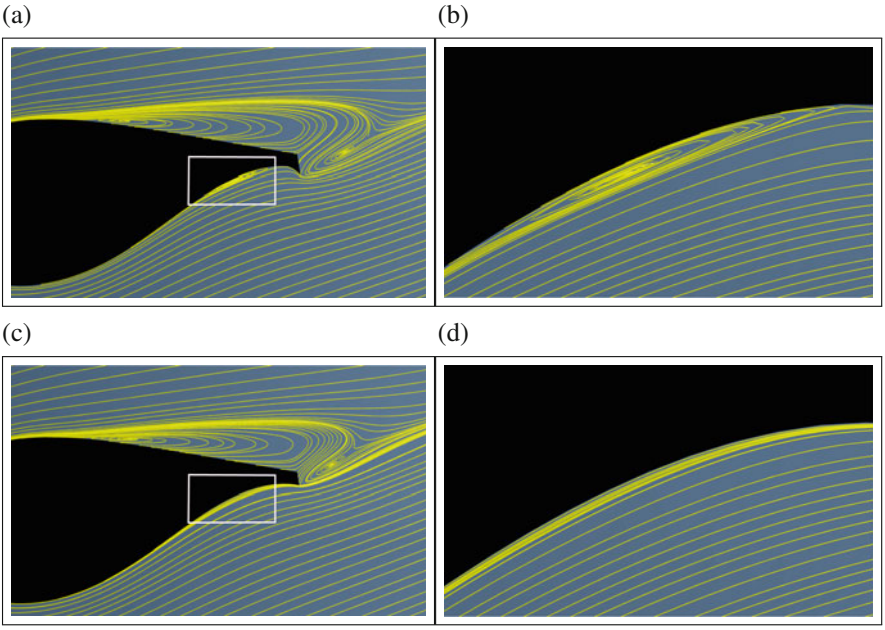

Fig. 18.9 Cross-section streamlines for $r = 23$ m at *rated speed*. *Rigid* simulations. (**a**) *G* (*Gurney*), global view. (**b**) *G* (*Gurney*), pressure side zoom. (**c**) *NG* (*no-Gurney*), global view. (**d**) *NG* (*no-Gurney*), pressure side zoom

for the first modes. As an example a difference up to 6.12 % was found for the first mode at 9.6 RPM.

In order to check if the *Gurney flaps* flow control mechanism illustrated in Fig. 18.6 was reproduced in the DTU 10 MW RWT geometry, a detailed analysis of the *rigid* configuration at *rated* speed was performed. Figure 18.9 shows a comparison of the cross-section streamlines at $r = 23$ m. The generation of the pressure surface separation bubble was visible for the *G* configuration. A detailed view of this phenomenon is included in Fig. 18.9b. The suppression of the suction surface recirculation, expected after the installation of the *Gurney flaps*, was not observed. This behaviour was found for the whole low span range, as it can be deduced from the comparison of blade surface streamlines of Fig. 18.10a and b. Indeed, the removal of the *Gurney flaps* led to a slight decrease of the maximum radius of the suction surface separation (passing from 39.7 m for *G* to 38.1 m for *NG*). In addition, the flow around the pressure surface of *NG* remained attached for the whole blade span, except for a small recirculation bubble located at $r = [14.9, 20.3]$ m (see Fig. 18.10d). A similar flow pattern was observed for all the operating points of Table 18.2.

The benefits of the *no-Gurney NG* configuration on flow behavior had a direct impact on global rotor performance. Figure 18.11a and b show the global thrust

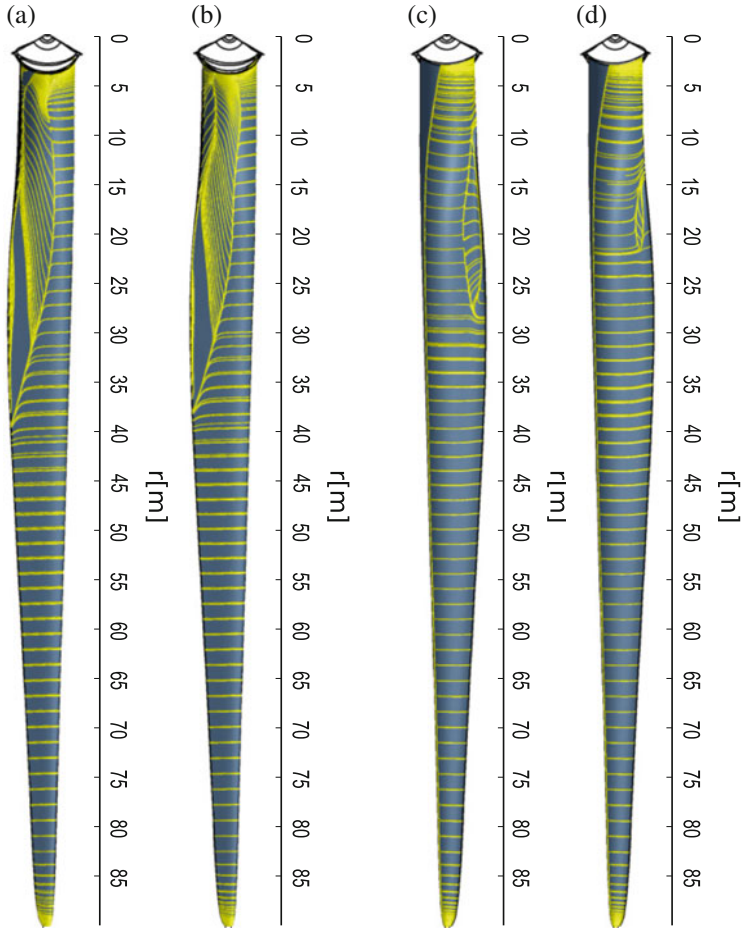

Fig. 18.10 Friction streamlines at *rated speed* for suction and pressure surfaces (referred as *SS* and *PS* respectively). *Rigid* simulations of *G* (*Gurney*) and *NG* (*no-Gurney*) configurations. (**a**) *SS-G*. (**b**) *SS-NG*. (**c**) *PS-G*. (**d**) *PS-NG*

and mechanical power coefficients, computed for both *G* and *NG* configurations. The results for *rigid* and *flexible* blade models are included. Global load coefficients were computed based on the following equations:

$$C_{t,global} = \frac{BT}{0.5\rho U_{\infty}^2 \pi R^2} \, , C_{p,global} = \frac{B\tau\Omega}{0.5\rho U_{\infty}^3 \pi R^2} \, , \tag{18.1}$$

Where T stands for the thrust force generated per blade, τ is the torque per blade, B stands for the number of blades, U_{∞} is the incoming fluid speed, ρ is the fluid density, R is the total blade span and Ω is the rotating speed.

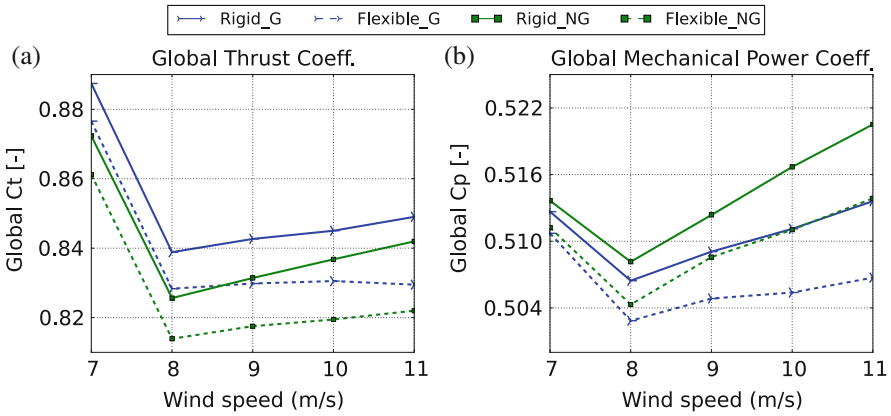

Fig. 18.11 Global load coefficients in function of wind speed for *G* (*Gurney*) and *NG* (*no-Gurney*) configurations. (**a**) Global thrust coefficient. (**b**) Global mechanical power coefficient

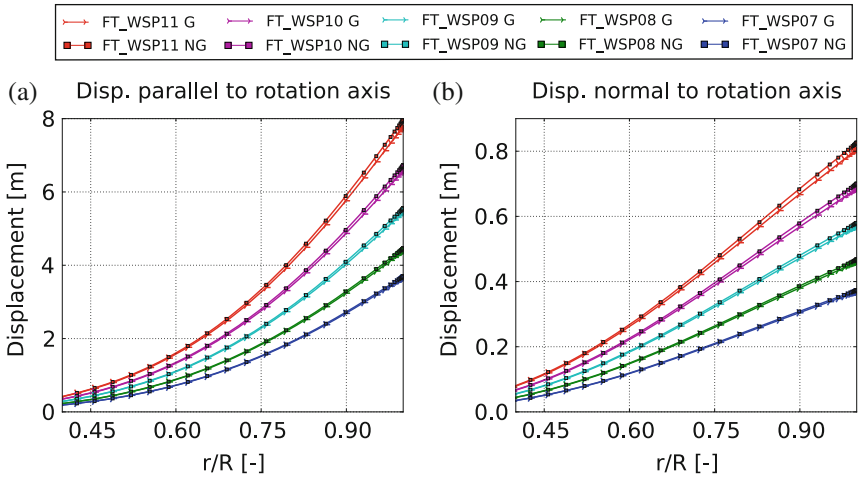

Fig. 18.12 DTU 10 MW RWT blade deformation in function of normalized radius. *G* (*Gurney*) and *NG* (*no-Gurney*) configurations. (**a**) Blade axis displacement parallel to rotor axis. (**b**) Blade axis displacement normal to rotor axis

At *rated speed* and for the *rigid* blade model, the installation of *Gurney flaps* decreased the mechanical power of 1.4 %, while the thrust was increased of 0.8 %. A similar trend was observed for lower wind speeds. Same remarks concerning the efficiency of *Gurney flaps* could be made when considering blade elasticity.

A global thrust and mechanical power decrease was observed for both *G* and *NG* configurations when considering aeroelasticity. This is related to the important blade deflections experienced by the blade. Figure 18.12 displays the

computed displacements parallel and normal to the rotor axis (often referred as out-of-rotor plane and in-rotor plane respectively). No significant differences were observed between the deflections corresponding to *G* and *NG* geometries. For both configurations, deformation parallel to rotor axis reached the 44 % of the blade tip/tower distance (18.26 m) at the *rated speed* operating point.

Based on the presented results, a decrease of the performance of the DTU 10 MW RWT rotor is expected after the integration of the *Gurney flaps*. Other alternatives in order to avoid the observed flow separation can be found in the literature. In Gaunaa et al. (2013), the use of leading edge slats at low span regions $r/R = [0.8, 0.32]$ was studied. Troldborg et al. (2015) considered the installation of *vortex generators* in order to control flow separation.

18.2.3 Static Aeroelasticity, Impact of Prebending and Preconing

The distance between the blade tip and the tower is often referred in the wind energy context as the *tower clearance*. In order to increase this gap (especially when dealing with large rotors), wind turbine designers use to introduce three geometrical considerations on the assembly:

- **Tilt angle**: Angle between rotor axis and tower
- **Precone angle**: Angle between blade axis and rotor axis
- **Prebending**: Blade deflection towards the incoming wind direction imposed during the blade design stage

The DTU 10 MW RWT accounts for all of them, as shown in Fig. 18.13a, where a sketch from the definition document of Bak et al. (2013) is reproduced. The geometrical effects of *prebending*, *tilt* and *preconing* are highlighted. In an operating wind turbine, the combination of all these modifications will try to align the deformed blade with the tower, as shown in Fig. 18.13b.

The aim of this section is to analyze how these geometrical considerations will impact rotor performance. The results of the already studied *straight* configuration were compared against a new and more *realistic* variant, accounting for *tower clearance* increase devices. Based on the conclusions of Sect. 18.2.2, new simulations were based on a blade geometry without *Gurney flaps*. In order to explore the whole 0° operating range of the machine, the load cases from Table 18.2 were analyzed again and compared with the *straight-NG* configuration results. Both *rigid* and *flexible* blades were analyzed.

A new mesh was generated with the same characteristics as the one described in Sect. 18.2.1. Since the introduction of the tilt angle was not compatible with the angular periodicity hypothesis, only the *prebending* and the *preconing* were considered. Based on the design specifications from Bak et al. (2013), the new

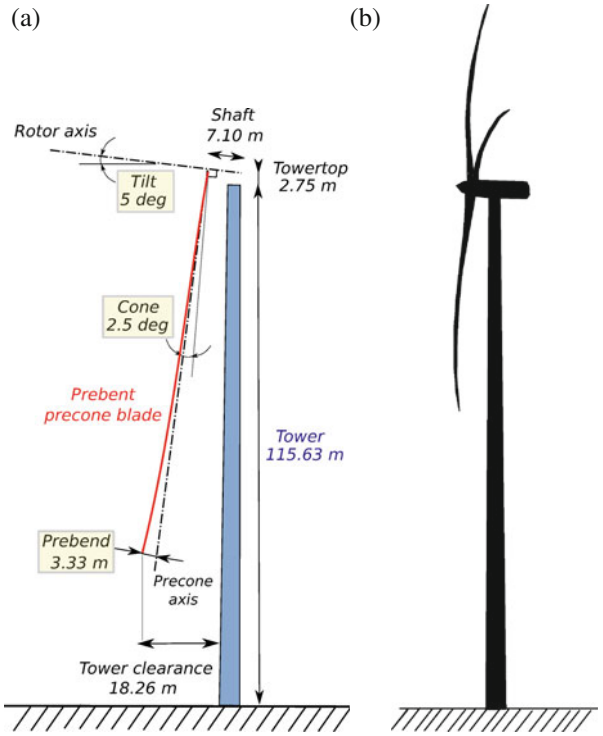

Fig. 18.13 Examples of whole wind turbine assemblies. (**a**) Sketch of the DTU 10 MW RWT assembly. (**b**) Representative sketch of a working wind turbine

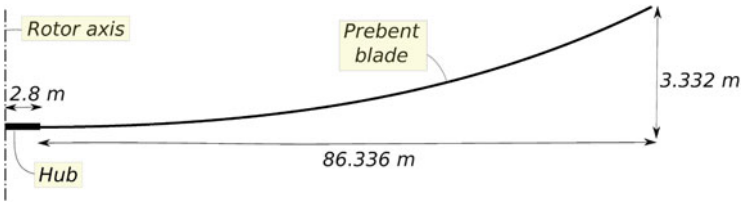

Fig. 18.14 DTU 10 MW RWT axis prebending definition, (reproduced from Bak et al. 2013)

considered geometry was generated by the application of the following geometrical operators on the standard DTU 10 MW RWT configuration:

1. Application of the prebending law definition on the *straight* blade (see Fig. 18.14)
2. Application of the 2.5° precone angle to the already prebent blade

Due to the significant geometrical modifications performed on the new *prebent-precone* blade, a new set of natural structural frequencies and mode shapes was required. The methodology described in Sect. 18.2.2 was used in order to perform

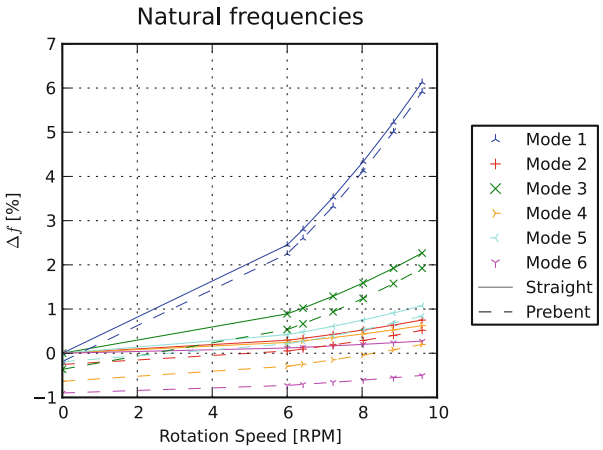

Fig. 18.15 Evolution of DTU 10 MW RWT blade frequencies in function of rotational speed, *straight* and *prebent-precone* blades (first six modes plotted)

Fig. 18.16 DTU 10 MW RWT modal analysis initial deformation (*blue-yellow*), superposed to the blade geometry reference (*red*) at *rated speed*. (**a**) Straight blade. (**b**) Prebent-precone blade

modal analysis for each one of the considered RPM. The same blade modes identified for the *straight* blade were observed for the new geometry. As previously shown in Fig. 18.8 for the *straight* configuration, a small RPM dependency was observed. In Fig. 18.15, the relative variations of natural frequencies corresponding to both configurations are compared. They are normalized by the frequency of the non-rotating *straight* blade. The evolutions of the frequencies with the rotation speed were very similar. Only a constant shift between *straight* and *prebent-precone* configuration was observed. This shift tended to increase with the mode number.

A more significant difference was related to the *centrifugal effects* included in the performed modal analysis. Indeed, an important *initial deformation* was observed for the *prebent-precone* configuration, due to offset of the blade geometry. In Fig. 18.16, the initial deformation (in blue-yellow) is superposed to the corresponding blade geometries (in red) for the *rated speed* operating point. While no difference was visible for the *straight* configuration (Fig. 18.16a), the *centrifugal effects* tended to straighten up the blade (Fig. 18.16b). As performed in the previous

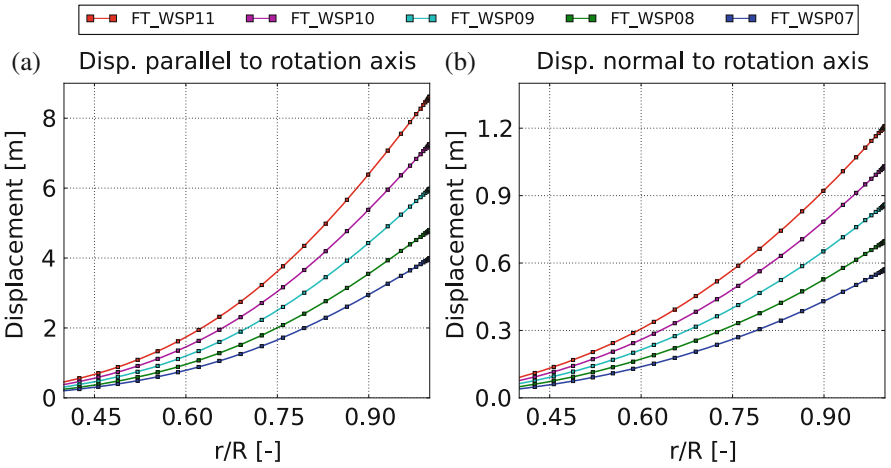

Fig. 18.17 DTU 10 MW RWT blade deformation in function of normalized radius for the *prebent-precone* configuration. (**a**) Blade axis displacement parallel to rotor axis. (**b**) Blade axis displacement normal to rotor axis

section, only the first six frequencies of the computed modal basis were used to model blade flexibility in the simulations.

Figure 18.17 shows the blade deformations for the *flexible* simulations of the *prebent-precone* rotor. Computed deformations were slightly higher than the ones corresponding to the *straight* rotor and previously displayed in Fig. 18.12. However, higher deformed blade tip/tower distances were observed for the *prebent-precone* configuration, due to its more conservative initial *tower clearance*. In order to illustrate this fact, Fig. 18.18 shows the reference (i.e. undeformed) and deformed blade axis coordinates for each of the presented aeroelastic computations. A global view is provided as well as a close zoom in order to properly contextualize the magnitude of the deformations. For the *prebent-precone* configuration, a blade tip/blade root alignment was observed for for the $10\,\mathrm{m\,s^{-1}}$ simulation. This operating point is indeed very close to the *rated speed* of the machine, verifying the prebending law defined at the design stage.

Computed global mechanical power coefficients of *straight* and *prebent-precone* configurations are shown in Fig. 18.19, together with a diagram superposing reference and deformed rotor geometries at *rated speed*. When considering the blades as *rigid*, a decrease in power was observed when introducing blade *prebending* and *preconing*. For the *straight* rotor, accounting for blade flexibility led to a reduction of the total power. This trend was reversed for the *prebent-precone* configuration, since the effect of flexibility tended to deform the blade towards a more orthogonal geometry with respect to the incoming flow (Fig. 18.19b). At *rated speed*, the power produced by the *flexible prebent-precone* blade was very close to the one computed for the *rigid straight* blade. An analogous plot regarding rotor global

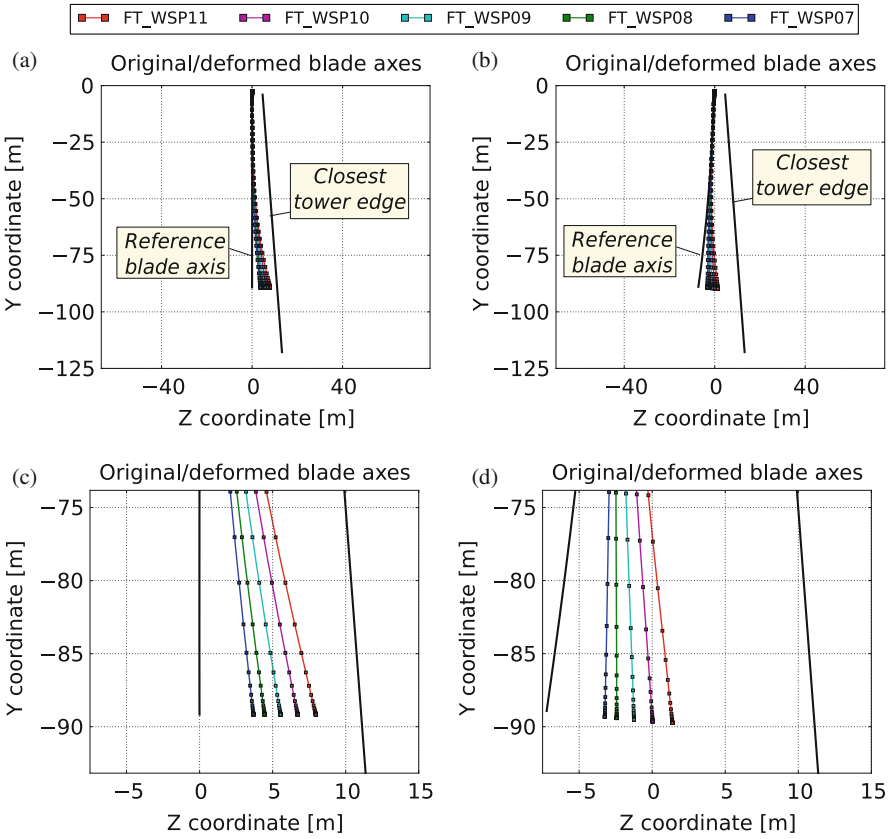

Fig. 18.18 Reference and deformed DTU 10 MW RWT blade axis coordinates with respect to closest tower edge. (**a**) *Straight* rotor (global view). (**b**) *Prebent-precone* rotor (global view). (**c**) *Straight* rotor (zoom). (**d**) *Prebent-precone* rotor (zoom)

thrust coefficient is included in Fig. 18.20. Lower thrust values were computed for the *prebent-precone* configuration with respect to the *straight* rotor. No significant differences between *flexible* and *rigid* simulations were observed for the *prebent-precone* configuration.

As a global conclusion, presented results show that aeroelastic analysis of DTU 10 MW RWT cannot be performed without considering the *prebending* and the *preconing* of the blades. Indeed, even if it does not largely affect the natural frequencies of the blade, its shape modification influences the performances of the wind turbine.

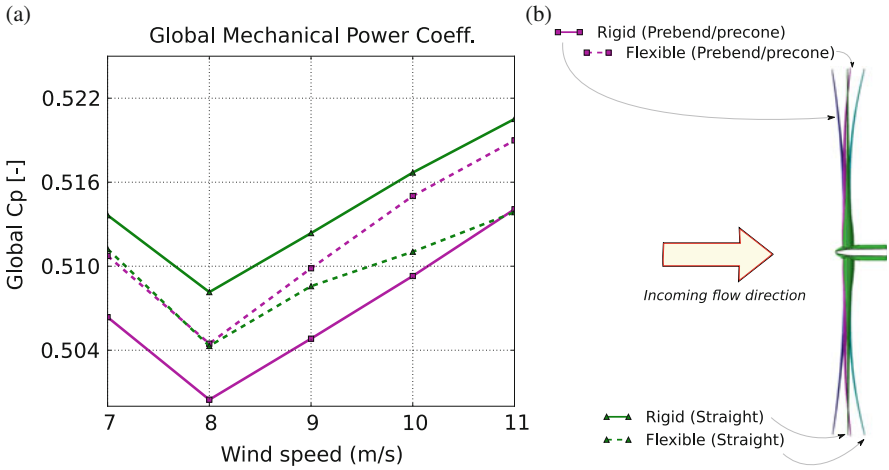

Fig. 18.19 Mechanical power coefficient of the DTU 10 MW RWT rotor, effects of *prebending-preconing* and flexibility. (**a**) Global mechanical power coefficient. (**b**) View of deformed blades at *rated speed*

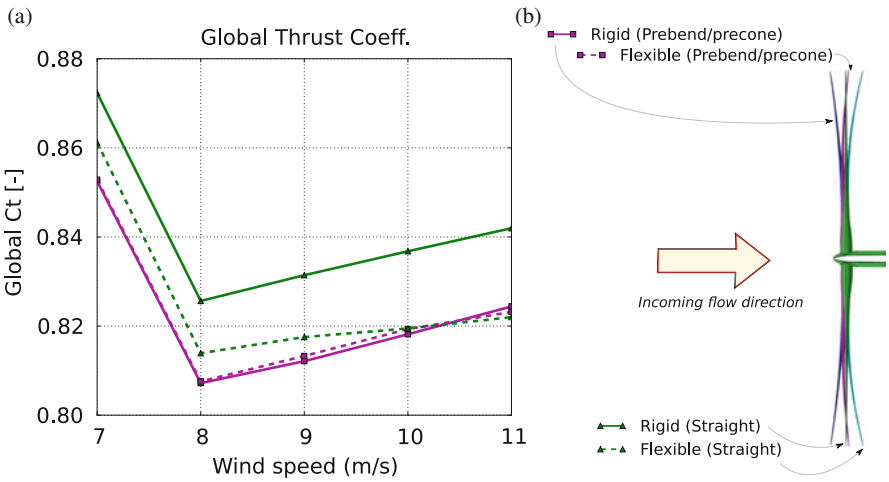

Fig. 18.20 Global thrust coefficient of the DTU 10 MW RWT rotor, effects of *prebending-preconing* and flexibility. (**a**) Global thrust coefficient. (**b**) View of deformed blades at *rated speed*

18.3 DTU 10 MW RWT Rotor-Tower Interactions Analysis

In this section, flow complexity was increased by considering the DTU 10 MW RWT tower in the computational domain. This more realistic scenario introduced an important unsteadiness in the flow due to the so-called *rotor-tower*

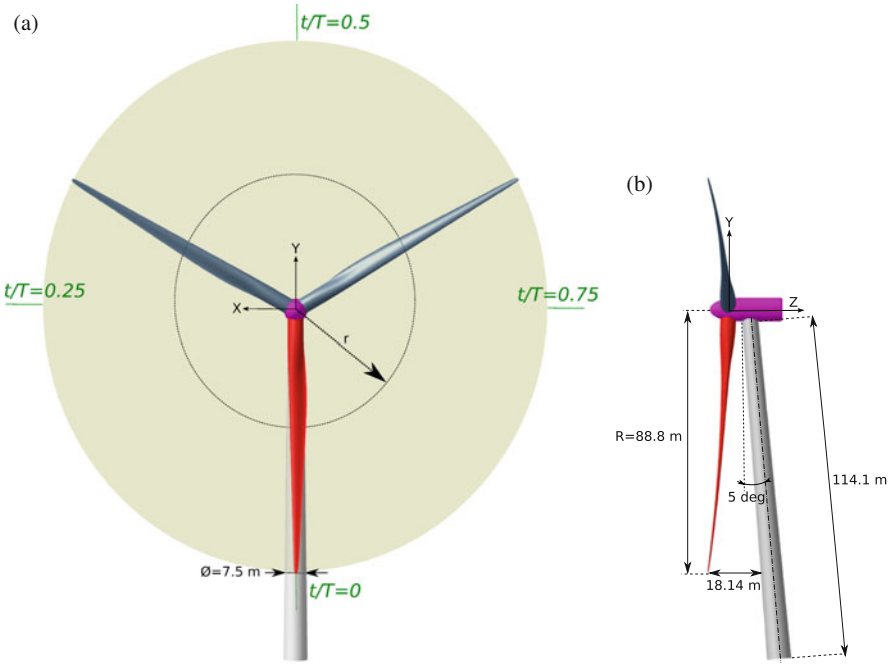

Fig. 18.21 Sketch of the DTU 10 MW RWT assembly. (**a**) Front view. (**b**) Side view

interactions. Hence, the use of more sophisticated numerical methods was required. In particular, the *Non-linear Harmonic* (NLH) approach presented by Vilmin et al. (2006) was used. In the NLH method, unsteady flow perturbations are Fourier decomposed. Navier-Stokes equations are then cast in the frequency domain, leading to the extraction of a set of transport equations for each harmonic. A single *blade passage* mesh is required. As a first approach and in order to keep the rotational periodicity of the problem, the incoming wind was assumed to be aligned with rotor axis. The hypothesis of *rigid* rotor blades was also made. The studied operating point was characterized by the following parameters:

- **Incoming wind speed:** 10.5 m s^{-1}
- **Rotor speed:** 8.836 RPM
- **Blade pitch:** 0°

Figure 18.21 illustrates the main geometrical properties of the studied DTU 10 MW RWT assembly, based on its definition from Bak et al. (2013). The rotor axis was co-linear with Z axis. A *tilt angle* of 5° was considered between rotor and tower axes. Blades accounted for a *precone* angle of 2.5° as well as a distributed *prebending*. Based on the disadvantageous effects on rotor performance found in Sect. 18.2.2, *Gurney flaps* were removed from blade geometry. In order to present the unsteady results of this section, the normalized time t/T was used. In this context, t is defined

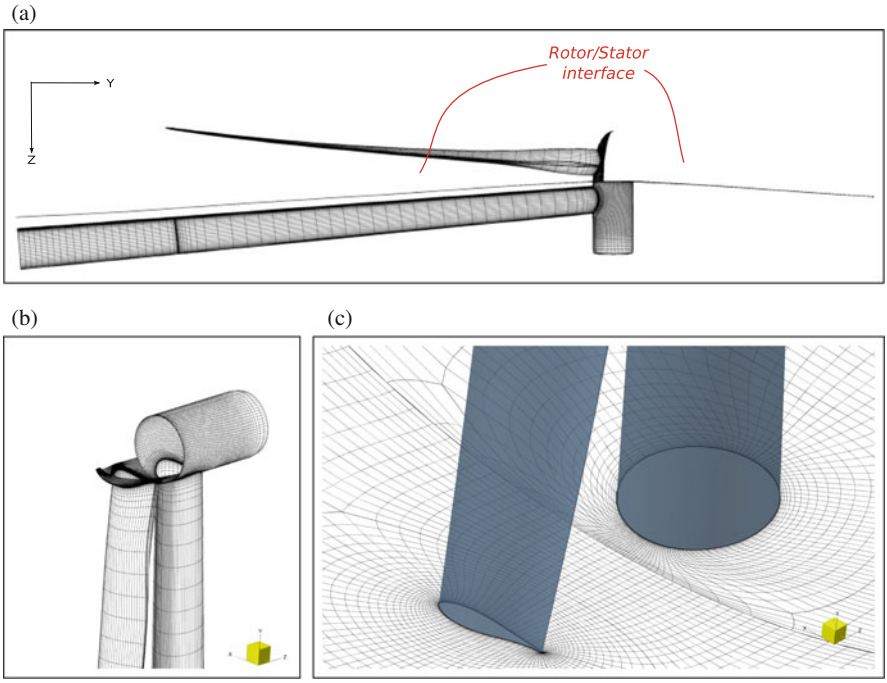

Fig. 18.22 DTU 10 MW RWT assembly mesh, 1 out of 2 mesh lines are skipped. (**a**) Surface mesh, global view. (**b**) Surface mesh, rotor detail. (**c**) Half-span cross-section grid line

as the already lapsed time in the current revolution and T refers to the period of rotation. The DTU 10 MW RWT operates in clockwise rotation, and it was assumed that at $t/T = 0$ one of the blades was aligned with the tower axis. This particular blade, displayed in red in Fig. 18.21, is referred in this document as the *observed blade*.

To generate a suitable mesh for NLH computations, DTU 10 MW RWT blade sections defined in Bak et al. (2013) were imported in Autogrid5™ structured grids generator (NUMECA International 2013a). Original nacelle, hub and tower geometries were also considered in the mesh generation process. To properly describe the boundary layer for the considered operating point, a first cell size of 3.0×10^{-5} m was imposed around the blade. A *rotor/stator interface* crossing the DTU 10 MW RWT nacelle was defined in order to connect rotating and non-rotating computational domains. A single *blade passage* was meshed in the rotor side, while a 360° grid was generated for the tower (or *stator*) region. Flow inlet and outlet were located at 2.2 and 3.2 blade radius from the nacelle, respectively. Figure 18.22 shows the complete generated mesh, accounting for 13 millions of nodes. For clarity purposes, 1 out of 2 mesh lines were skipped.

A total of nine harmonics were considered. The Spalart–Allmaras turbulence model (Spalart and Allmaras 1992) was used. A full non-matching non-reflecting

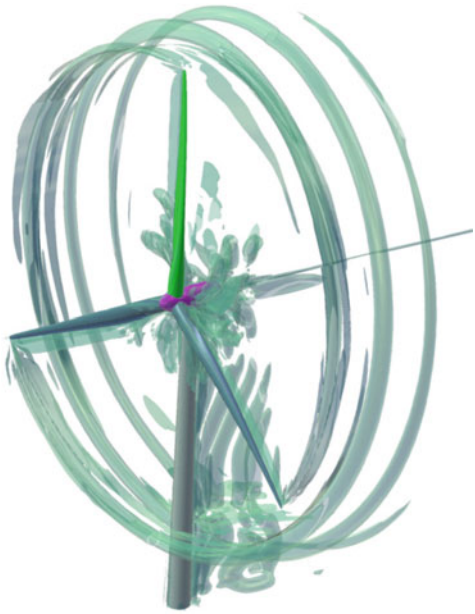

Fig. 18.23 Iso-surface of 0.5 Q-criterion at $\frac{t}{T} = 0.50$

approach was employed for the modeling of the *rotor/stator interface* (Vilmin et al. 2006). First resolved rotor harmonic was located at 0.15 Hz, corresponding to the rotational speed at the considered operating point. Since the DTU 10 MW RWT has a three-bladed rotor, a frequency of 0.45 Hz was observed for the first tower harmonic. Even if flow variables are solved in the frequency domain, NLH results can be easily reconstructed in time in order to perform a more comprehensive postprocessing. This process is referred in this document as the *time solution reconstruction*.

The complexity of this unsteady problem could be already pointed out with the visualization of the flow at a given time. Figure 18.23 illustrates the iso-surfaces of Q-criterion for a value of 0.5 of the time reconstructed solution at $\frac{t}{T} = 0.50$. Important vortical structures could be observed downstream of the tower. These were present all along the tower height. High vorticity regions were identified at low blade span range (where the DTU 10 MW RWT is equipped with thicker airfoils). The generation of blade tip vortex was clearly visible. The collision of this structure with the tower led to an important increase of downstream vorticity.

The observed vorticity at low blade span can be related to the *shedding* phenomenon. Figure 18.24 shows the streamlines around the *observed blade* for a $r = 20\,m$ cross-section. Indeed, the low span suction side recirculation already identified for the *rotor-only* RANS computations was shed from the blade. This effect was especially visible when the blade approached the tower (i.e. for $\frac{t}{T} = 0.00$ and $\frac{t}{T} = 0.76$). A similar *vortex shedding* phenomenon was identified downstream of the tower all along its height.

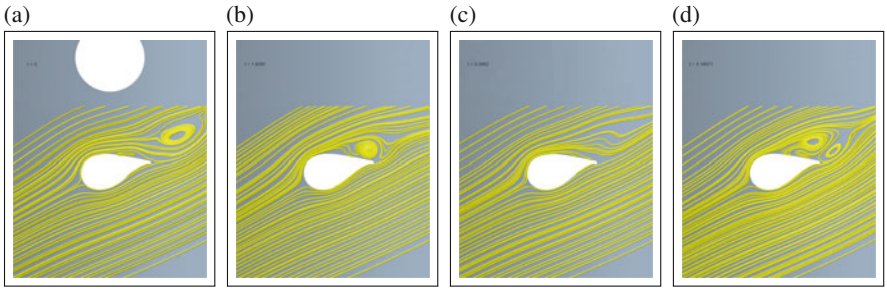

Fig. 18.24 Relative velocity streamlines around the *observed blade* for a $r = 20$ m cross-section. (**a**) $\frac{t}{T} = 0.00$. (**b**) $\frac{t}{T} = 0.24$. (**c**) $\frac{t}{T} = 0.50$. (**d**) $\frac{t}{T} = 0.76$

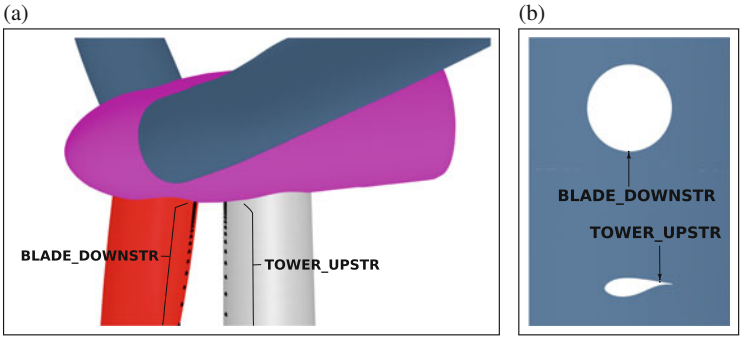

Fig. 18.25 Location of BLADE_DOWNSTR and TOWER_UPSTR sets of sensors. (**a**) DTU 10 MW RWT front view. (**b**) Cut at $r = 44.5$ m

When characterizing the frequency content of the blade *shedding*, an important spanwise dependency was observed. Two sets of sensors were defined in order to have an overview of this relation: BLADE_DOWNSTR and TOWER_UPSTR, both installed all along a mesh line. While BLADE_DOWNSTR was positioned at the observed blade *shedding* location, TOWER_UPSTR intended to analyze the impact of the rotor perturbation on the tower (see Fig. 18.25).

Figure 18.26 illustrates the harmonic pressure amplitudes for every point included in BLADE_DOWNSTR and TOWER_UPSTR. The results are expressed as a function of the considered harmonic (referenced here as *Harmonic order*), and of the radial position of each point. The blade *shedding* phenomenon could be identified for BLADE_DOWNSTR at the vicinity of 20 m. In this region, important harmonic amplitudes corresponding to the fifth harmonic were observed. The influence of *blade shedding* on the tower was visible in TOWER_UPSTR, where a shifting of the harmonic content towards higher frequencies was observed at low span.

Figure 18.27 shows rotor loads time evolution, where the effects of the *blade-tower alignment* event are clearly visible at $\frac{t}{T} = 0, \frac{1}{3}, \frac{2}{3}$. The corresponding result

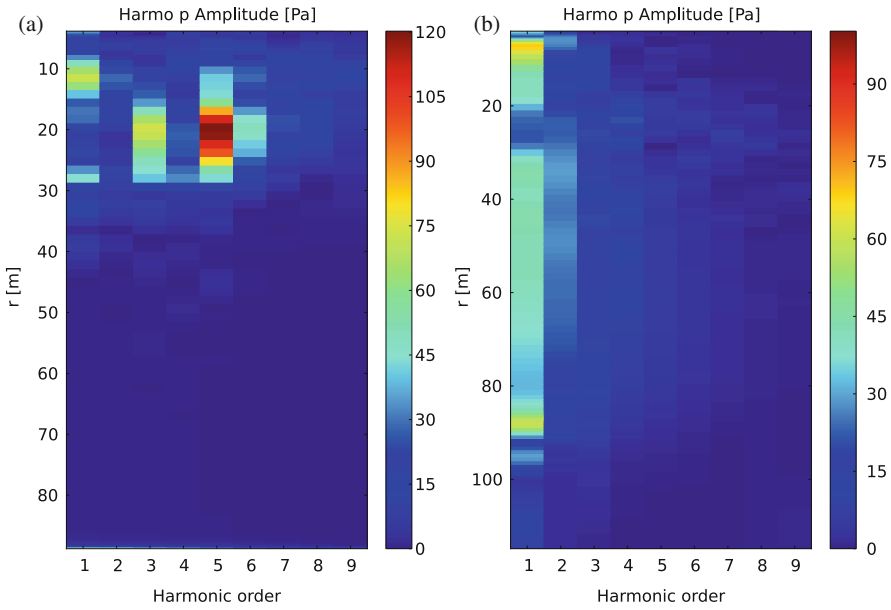

Fig. 18.26 Harmonic pressure amplitude [Pa] for the defined sets of sensors, as a function of r [m]. (**a**) BLADE_DOWNSTR. (**b**) TOWER_UPSTR

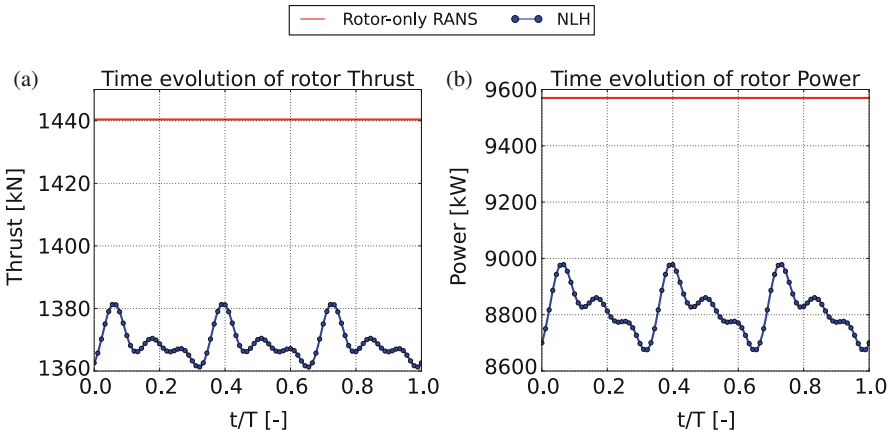

Fig. 18.27 DTU 10 MW RWT rotor loads as a function of normalized time. (**a**) Thrust [kN]. (**b**) Power [kW]

for a *rotor-only* RANS simulation based on the set-up of Sect. 18.2 is included for reference. Relative loads fluctuation amplitudes of 1 % for the rotor thrust and 2 % for the mechanical power were computed. The presence of the tower led to a time-averaged decrease of 5 % of rotor thrust and 8 % of mechanical power with

respect to the corresponding *rotor-only* simulation. Therefore it can be concluded that the influence of the tower is not negligible when assessing the wind turbine performance.

18.4 Conclusions and Future Work

A numerical analysis of the DTU 10 MW RWT *reference* wind turbine aerodynamics was presented and discussed. A three-dimensional CFD-based methodology was developed in order to tackle two challenging problems. On one hand, the impact of large OWT blade deflections on rotor performance (the so-called *aeroelastic effects*). On the other hand, the modeling of flow unsteadiness coming from the consideration of the tower in the CFD set-up (also referred as *rotor-tower interactions*).

The issue of aeroelasticity was studied in a *rotor-only* framework. First simulations aimed to verify the obtained results for a *straight* and *rigid* configuration regarding to CFD simulations performed by other authors. For both methodologies, computed flow separation and rotor loads were in good agreement. After this initial comparison the developed tool was extended by including a structural model of the blade, represented by its natural frequencies and deformed shapes. This enhanced numerical approach was used in order to study the influence of two different geometrical modifications of the blade on final rotor performance and aeroelastic response. First, the impact of *Gurney flaps* installation was discussed. No re-attachment of the suction surface separation bubble was observed after the introduction of these devices, and a wider pressure surface recirculation zone was identified. The evaluation of the total mechanical power and thrust showed that *Gurney flaps* reduced the global performance of the DTU 10 MW RWT rotor for the considered operating points. This remark could be made for both *rigid* and *flexible* configurations. For the latter case blade tip deformations of 8 m were computed at *rated speed*, leading to a power production decrease of 1.4 %. It can be concluded that the consideration of blade *flexibility* is necessary in order to properly estimate the final rotor performance. Secondly, the results of a *prebent-precone* rotor were compared with the standard *straight* configuration. When considering the blades as *rigid*, the combination of both geometrical modifications led to a decrease of the computed rotor loads. At *rated speed*, reductions of 1 % of thrust and 2 % of mechanical power were observed. When analyzing the corresponding *flexible* blade configurations, the effect of aeroelasticity on rotor performance was reversed. Indeed, while a reduction in the generated power was observed for the deformed *straight* rotor, an increase was found for the *prebent-precone* configuration. This inversion was explained by the deformed rotor geometries, since for the *prebent-precone* simulations the blade flexibility tended to recover the orthogonality with respect to the incoming flow. These results show that aeroelastic analysis of DTU 10 MW RWT cannot be performed without considering the *prebending* and the *preconing* of the blades.

Finally, the NLH method was applied in order to study the whole DTU 10 MW RWT assembly (including the tower). This approach was able to capture the complex unsteady aerodynamics related to *rotor-tower interactions*. The presence of the tower had a direct impact on rotor performance, justifying the numerical analysis of the *full machine*. Decreases of around 5 % of time-averaged rotor thrust and 8 % of power were computed. These reductions are in line with previous studies based on other wind turbines (Hsu and Bazilevs 2012; Hsu et al. 2014; Carrión 2014; Li 2014). Local unsteady flow patterns around the whole DTU 10 MW RWT assembly were also characterized. In particular, both tower and blade *shedding* phenomena were identified. The latter effect was found to be related to high frequencies. In particular, the considered operating point revealed a blade *shedding* frequency corresponding to the fifth harmonic. This harmonic order is coherent with the results of previous CFD computations of the NREL Phase VI (Le Pape and Lecanu 2004; Li 2014). Regarding the *blade-tower alignment* event, loads fluctuation relative amplitudes of 1 % for the rotor thrust and 2 % for the mechanical power were computed.

Future work will be devoted to extend the capabilities of the NLH method to account for a structural model of the blades, in order to assess the combined impact of rotor flexibility and flow unsteadiness on rotor performance. Additionally, the studied DTU 10 MW RWT operating range will be extended to higher wind speeds to evaluate the performance of the presented methodology when considering more important angles of attack.

Acknowledgements The authors acknowledge the *European Commission* for their research grant under the project FP7-PEOPLE-2012-ITN 309395 *MARE—WINT* (*new MAterials and REliability in offshore WINd Turbines technology*), as well as all the members from FINE™/Turbo team of NUMECA International for their valuable and active contribution.

References

Bak C, Zahle F, Bitsche R, et al (2013) The DTU 10-MW reference wind turbine. In: DTU orbit - the research information system. Available via Technical University of Denmark. http://orbit.dtu.dk/files/55645274/The_DTU_10MW_Reference_Turbine_Christian_Bak.pdf. Accessed 08 Apr 2016

Carrión M (2014) Low Mach number CFD for wind turbine analysis. Dissertation, University of Liverpool

Corson D, Griffith DT, Ashwill T, et al (2012) Investigating aeroelastic performance of multi-mega watt wind turbine rotors using CFD. Paper presented at the 53rd AIAA/ASME/ASCE/AHS/ASC structures, structural dynamics and materials co-located conferences, Honululu, 23–26 April 2012

Debrabandere F (2014) Computational methods for industrial fluid-structure interactions. Dissertation, Université de Mons (UMONS)

Elfarra MA, Sezer-Uzol N, Akmandor IS (2014) NREL VI rotor blade: numerical investigation and winglet design and optimization using CFD. Wind Energy 17(4):605–626

Fan Z, Kang S (2009) Numerical simulations of the aerodynamics performance of Horizontal Axis Wind Turbines. In: Tao Y, Ma C (eds) UECTC 2009. Inaugural US-EU-China thermophysics conference-renewable energy, Beijing, May 2009. American Society of Mechanical Engineers (ASME), Houston. doi:10.1115/1.802908.paper16

Gaunaa M, Zahle F, Sørensen NN, et al (2013) Rotor performance enhancement using slats on the Inner part of a 10 MW rotor. Paper presented at the European wind energy conference and exhibition (EWEA), Vienna, 4–7 February 2013

Heege A, Gaull A, Horcas SG, et al (2013) Experiences in controller adaptations of floating wind turbines through advanced numerical simulation. Paper presented at the AWEA WINDPOWER 2013 conference and exhibition, Chicago, 5–8 May 2013

Horcas SG, Debrabandere F, Tartinville B, et al (2014) Mesh deformation tool for Offshore Wind Turbines fluid-structure interaction. In: Abstracts of the 11th World Congress on Computational Mechanics (WCCM XI), Barcelona, 20–25 July 2014

Horcas SG, Debrabandere F, Tartinville B, et al (2015a) A new, high fidelity offshore wind turbines aeroelasticity prediction method with significant CPU time reduction. Poster presented at the Offshore 2015. European Wind Energy Association, Copenhagen, 10–12 March 2015

Horcas SG, Debrabandere F, Tartinville B, et al (2015b) Hybrid mesh deformation tool for offshorewind turbines aeroelasticity prediction. In: Ferrer E, Montlaur A (eds) CFD for wind and tidal offshore turbines SE - 8, Springer tracts in mechanical engineering. Springer, Heidelberg, pp 83–94

Hsu MC, Bazilevs Y (2012) Fluid-structure interaction modeling of wind turbines: simulating the full machine. Comput Mech 50(6):821–833

Hsu MC, Akkerman I, Bazilevs Y (2014) Finite element simulation of wind turbine aerodynamics: validation study using NREL Phase VI experiment. Wind Energy 17:461–481

Jonkman JM, Buhl ML (2007) Development and verification of a fully coupled simulator for offshore wind turbines, NREL/CP-500-40979. In: National Renewable Energy Laboratory documents. Available via NREL. http://www.nrel.gov/docs/fy07osti/40979.pdf. Accessed 11 Apr 2016

Larsen T, Hansen A (2007) How to HAWC2, the User's manual. In: DTU orbit - the research information system. Available via Technical University of Denmark. http://orbit.dtu.dk/files/7703110/ris_r_1597.pdf. Accessed 11 Apr 2016

Le Pape A, Lecanu J (2004) 3D Navier-Stokes computations of a stall-regulated wind turbine. Wind Energy 7(4):309–324

Li Y (2014) Coupled computational fluid dynamics/multibody dynamics method with application to wind turbine simulations. Dissertation, University of Iowa

Liebeck RH (1978) Design of subsonic airfoils for high lift. J. Aircraft 15(9):547–561

Lynch CE (2011) Advanced CFD methods for wind turbine analysis. Dissertation, Georgia Institue of Technology

NUMECA International (2013a) Autogrid5™ v9.0 User Manual, NUMECA, Brussels

NUMECA International (2013b) FINE™/Turbo v9.0 User Manual, NUMECA, Brussels

Simulia DSC (2008) Abaqus Analysis version 6.8 User's Manual, Simulia, Waltham

Sørensen NN (1995) General purpose flow solver applied to flow over hills. Risø National Laboratory, Roskilde

Spalart P, Allmaras S (1992) A one-equation turbulence model for aerodynamic flows. In: Abstracts of the 30th AIAA aerospace sciences meeting and exhibit, AIAA, Reno, 6–9 January 1992

Suárez JM, Doerffer P, Szulc O (2015a) CFD validated technique for prediction of aerodynamic characteristics on horizontal axis wind energy turbines. Poster presented at the Offshore 2015. European Wind Energy Association, Copenhagen, 10–12 March 2015

Suárez JM, Doerffer P, Szulc O, et al (2015b) Aerodynamic analysis of wind turbine rotor blades. Task Quart 19(2):129–140

Troldborg N, Zahle F, Sørensen NN (2015) Simulation of a MW rotor equipped with vortex generators using CFD and an actuator shape model. In: 53rd AIAA Aerospace Sciences Meeting, American Institute of Aeronautics and Astronautics, Kissimmee, 5–9 July 2015

Vilmin S, Lorrain E, Hirsch C, et al (2006) Unsteady flow modeling across the rotor/stator interface using the nonlinear harmonic method. In: Abstracts of the ASME Turbo Expo 2006: power for land, sea and air, American Society of Mechanical Engineers, Barcelona, 8–11 May 2006

Wang Q, Zhou H, Wan D (2012) Numerical simulation of wind turbine blade-tower interaction. J Mar Sci Appl 11(3):321–327

Yu DO, Kwon OJ (2014) Predicting wind turbine blade loads and aeroelastic response using a coupled CFD-CSD method. Renewable Energy 70:184–196

Zahle F, Sørensen NN (2008) Overset grid flow simulation on a modern wind turbine. In: Abstracts of the 26th AIAA applied aerodynamics conference, guidance, navigation, and control and co-located conferences, American Institute of Aeronautics and Astronautics, Honolulu, 18–21 August 2008

Zahle F, Sørensen NN (2011) Characterization of the unsteady flow in the nacelle region of a modern wind turbine. Wind Energy 14(2):271–283

Zahle F, Sørensen NN, Johansen J (2009) Wind turbine rotor-tower interaction using an incompressible overset grid method. Wind Energy 12(6):594–619

Zahle F, Bak C, Guntur S, et al (2014) Comprehensive aerodynamic analysis of a 10 MW wind turbine rotor using 3D CFD. In: Abstracts of the 32nd wind energy symposium, American Institute of Aeronautics and Astronautics, National Harbor, 13–17 January 2014

Part VI
Offshore Wind Farm Design